Check for updates

# Current development, optimisation strategies and future perspectives for lead-free dielectric ceramics in high field and high energy density capacitors

Hareem Zubairi, [iD] [a] Zhilun Lu, [iD] *[b] Yubo Zhu,[c] Ian M. Reaney[c] and Ge Wang [iD] *[a]

To meet the United Nations' sustainable development goal of affordable and clean energy, there has been a growing need for low-cost, green, and safe energy storage technologies. High-field and energy-density capacitors have gained substantial attention from academics and industry, particularly for power electronics, where they will play a key role in optimising the performance of management systems in electric vehicles. The key figure of merit, energy density ($W_{rec}$), for high-field applications has dramatically increased year-on-year from 2020 to 2024, as evidenced by over 250 papers, demonstrating ever larger $W_{rec}$ values. This review briefly introduces the background and principles of high energy density ceramics, but its focus is to provide constructive and comprehensive insight into the evaluation of $W_{rec}$, $E_{max}$, $\Delta P$, and $\eta$, and more importantly, the normalised metrics, $W_{rec}/E_{max}$ and $W_{rec}/\Delta P$ in lead-free dielectric ceramics. We also present several optimisation strategies for materials modification and process innovation that have been recently proposed before providing perspectives for the further development of high-field and high-energy density capacitors.

[a] *Department of Materials, University of Manchester, Manchester, M13 9PL, UK. E-mail: ge.wang@manchester.ac.uk*
[b] *School of Chemical and Process Engineering, University of Leeds, Leeds, LS2 9JT, UK. E-mail: z.lu@leeds.ac.uk*
[c] *Department of Materials Science and Engineering, University of Sheffield, Sheffield, S1 3JD, UK*

Hareem Zubairi is a Dean's doctoral scholarship funded (2023) PhD student at the Department of Materials, The University of Manchester. She obtained her BSc in Materials Engineering (2019) and MSc (2022) specialising in cold sintering of multiferroic ceramics from NED University, Pakistan. Hareem's dedicated research delves deep into the structure-composition-property relationship of lead-free ferroelectric, dielectric and piezoelectric ceramics.

**Hareem Zubairi**

Dr Zhilun Lu is an Assistant Professor of Materials Science and Engineering at the University of Leeds. His research group focuses on the structure-composition-property relations of a broad spectrum of advanced functional materials, particularly ferroelectrics and thermoelectric. His expertise lies in employing impedance spectroscopy to probe electrical properties and neutron scattering to elucidate atomic structure and dynamics. He has led projects funded by the Royal Society and Royal Society of Chemistry, and published over 70 peer-reviewed papers, including in Nature Physics, garnering an H-index of 28. He is a frequent invited speaker at international conferences and serves on the editorial boards of several top materials science journals. He is also a peer reviewer for journals such as Nature Physics and Nature Communications.

**Zhilun Lu**

This journal is © The Royal Society of Chemistry 2024

*Chem. Soc. Rev.*, 2024, **53**, 10761–10790 | **10761**

# 1. Introduction

Global energy demand has been increasing rapidly due to industrialisation, technological advancements, and the expanding economies of countries. According to a recent International Energy Agency (IEA) report,[1] global energy consumption is expected to rise by 3.4% per year until 2026. To minimise global $CO_2$ emissions, renewable, smart, and clean energy systems with high energy storage performance must be rapidly deployed to achieve the United Nation's sustainability goal.[2] The energy density of electrostatic or dielectric capacitors is far smaller than in batteries and fuel cells.[3–5] However, they possess the highest power density due to ultra-fast charge–



Fig. 1 Power density *vs.* energy density (Ragone Plot) for different energy storage technologies.

discharge, as shown in the Ragone Plot (Fig. 1)[6–8] and form an integral part of the power management of battery systems.

$BaTiO_3$-based multilayer ceramic capacitors are commonly employed as filters and de-couplers in the consumer electronics industry, with a market valued at USD $\sim$ 3 billion in 2023, with a 4.9% compound annual growth rate in the US market (2024–2032).[7] Ceramic dielectrics are popular due to their temperature stability (*e.g.* X7R MLCCs),[9] fast charge–discharge speed (ms or ns), strong mechanical and fatigue resistance, and low manufacturing costs compared to polymer dielectrics.[10] However, $BaTiO_3$-based dielectrics break down at relatively low fields ($<350$ kV cm$^{-1}$), limiting their energy density, and above 130 °C their permittivity declines markedly.[10] Developing

**Yubo Zhu**

*Yubo Zhu received his bachelor's degree from the University of Sheffield, UK, in 2022. He is currently a Year 2 PhD student in Prof. Ian M Reaney's group specifically on energy storage functional materials, his research focuses on sodium niobate systems.*



**Ian M. Reaney**

*Prof. Ian M. Reaney holds the Dyson Chair in Ceramics at the Department of Materials Science and Engineering, the University of Sheffield. He is a Fellow of the American and European Ceramic Society, the Royal Microscopical Society and the Institute of Materials, Minerals and Mining (IOM3). He has won numerous awards including the Verulam Medal (2017) in Ceramics from IOM3 and was recently elected to the World Academy of Ceramics. He is an Adjunct Professor at Pennsylvania State University (PSU) and European site director of the Centre for Dielectrics and Piezoelectrics in partnership with PSU and North Carolina State University. He published over 400 scientific papers with > 27000 citations in total and H-index = 88 (Google Scholar). His research leadership in a wide range of ceramic disciplines has been recognised by > 90 Invited/Plenary talks at International Conferences on topics such as Net-zero technology for ceramic manufacture, cold-sintering, microwave ceramics, bioceramics, relaxor-ferroelectrics, capacitors and piezoelectrics.*



**Ge Wang**

*Dr Ge Wang obtained a PhD (2016) from the University of Manchester. He worked as a Postdoctoral research associate at the University of Sheffield (2017-2022) and recently was awarded a Dame Kathleen Ollerenshaw Fellowship (2022) at the Department of Materials, The University of Manchester. His research is focused on the development (synthesis and characterisation) of high-performance functional ceramics, including electroceramics, solid-state electrolytes and high entropy perovskite oxides, using skillset ranging from crystal chemistry and crystallography to advanced processing of ceramics and prototype devices. He published 40+ peer-reviewed articles with a H-index of 24 and > 3800 citations (Google Scholar). He is currently the deputy research lead for Nano and Functional Materials at the Department of Materials, a member of the early career editorial board for the Journal of Advanced Dielectric (JAD), and a professional member (MIMMM) of IOM3 and the Royal Society of Chemistry (MRSC).*

**10762** | *Chem. Soc. Rev.*, 2024, **53**, 10761–10790

This journal is © The Royal Society of Chemistry 2024

**Fig. 2** (a) Number of publications, Web of Science (keywords of high energy density ceramics, multilayer ceramic capacitors, and ceramic thin films, excluding glass, polymer, and composite). (b) Development of $W_{rec}$ in bulk ceramics, ceramic multilayers, and ceramic thin films for energy storage applications from 2015 to 2024.

next-generation dielectric ceramics with higher energy density for high-field/voltage and high temperature ($>200\ ^{\circ}$C) capacitor applications has therefore drawn increasing interest, particularly for power electronics in the automotive sector.

Lead (Pb) based dielectric ceramics, such as La-doped Pb(Zr, Ti)O$_3$,[11,12] have been used in pulsed capacitor applications for a number of years due to their exceptional power density and efficiency. However, researchers have been favouring Pb-free alternatives in the past decade due to legislation that restricts the use of Pb in consumer electronics. Fig. 2(a) illustrates the increase in publications on lead-free high-energy density ceramics from 2015 ($\sim 50$ papers) to 2023 ($\sim 500$ papers). Bulk ceramics based on BaTiO$_3$(BT), Na$_{0.5}$Bi$_{0.5}$TiO$_3$ (NBT), BiFeO$_3$ (BF), AgNbO$_3$ (AN) and NaNbO$_3$(NN)-based ceramics, account for 80% of the publications, with multilayer ceramic capacitors (MLCCs) 8% and ceramic thin films 12%.

The highest energy densities reported in the past 10 years for Pb-free bulk ceramics, MLCCs, and ceramic thin films are 16.3 J cm$^{-3}$, 43.5 J cm$^{-3}$, and 182 J cm$^{-3}$, respectively. These values are achieved with approximate thicknesses of 50–150 μm for bulk ceramics, 5–20 μm for MLCCs, and 0.1–0.6 μm for ceramic thin films, and electrode areas typically ranging from 0.075 to 0.12 cm$^2$. Bulk ceramics and MLCCs are prepared by solid-state sintering, with energy density influenced by factors such as electrode area and thickness. In contrast, ceramic thin films are formed using different techniques, where factors like substrate choice (strain), electrode area and thickness play a crucial role. However, further research in Pb-free dielectric ceramics is still required to offer high energy density ($W_{rec} > 20$ J cm$^{-3}$) with efficiency ($\eta > 90$%), wide frequency range (1–1000 Hz), large temperature range ($-50$ to 250 $^{\circ}$C), low dielectric loss (tan $\delta <$ 2.5%), fast charge–discharge time ($\tau_{0.9} < 100$ ns), co-fire compatibility with cost-effective internal electrodes and greater volumetric efficiency.

In the realm of energy storage capacitors, many companies such as Skelton Technologies, TDK, Taiyo Yuden, Panasonic Corporations, Maxwell Technologies (now part of Tesla, Inc.), Kyocera Corporation, Murata Manufacturing Co. Ltd, Knowles Capacitors, and Ioxus, offer bulk ceramics and MLCCs tailored to specific applications. For instance, Knowles Precision Devices manufactures a wide selection of MLCCs, including AEC-Q200, Tandem and Open Mode, X8R and EMI filters, to meet the needs of electric and hybrid electric vehicle systems with a maximum voltage rating of 1 kV.[13] Ceramic capacitor technology is expected to advance further with the MLCC market forecast to reach $\sim$ USD 16.77 billion by 2030.[14] High energy density and high voltage capacitors will be used in many applications[15] as shown in Fig. 3, including but not limited to power electronics in electrical transportation, electronics, aerospace, pulse power applications and solar plants due to their high voltage tolerance, low loss, greater temperature and frequency stability and volumetric efficiency.[9]

# 2. Principles of energy storage performance in lead-free dielectric ceramics

Understanding the principles of energy storage performance is crucial for designing and optimising materials for specific applications. The chapter covers three main topics: energy storage density evaluation, polarisation, and dielectric breakdown strength.

## 2.1. Energy density evaluation of dielectric ceramics

The typical representation of a capacitor consists of two parallel electrodes with a dielectric between them, as shown in Fig. 4(a and b). In dielectric capacitors, an external electric field is applied to induce polarisation in the dielectric, allowing for the storage of electrical energy (Fig. 4a). When the electric field is removed, the capacitor releases the stored energy, and the dipoles return to their initial state (Fig. 4b). This ability to store and release energy rapidly makes electrostatic capacitors suitable for applications requiring high power density ($P_D$) for applications requiring ultrafast charge–discharge ($\tau_{0.9}$) cycles.

This journal is © The Royal Society of Chemistry 2024

*Chem. Soc. Rev.*, 2024, **53**, 10761–10790 | **10763**

Fig. 3   Schematic diagram of MLCCs with key properties in developing the high energy performance and their different applications.
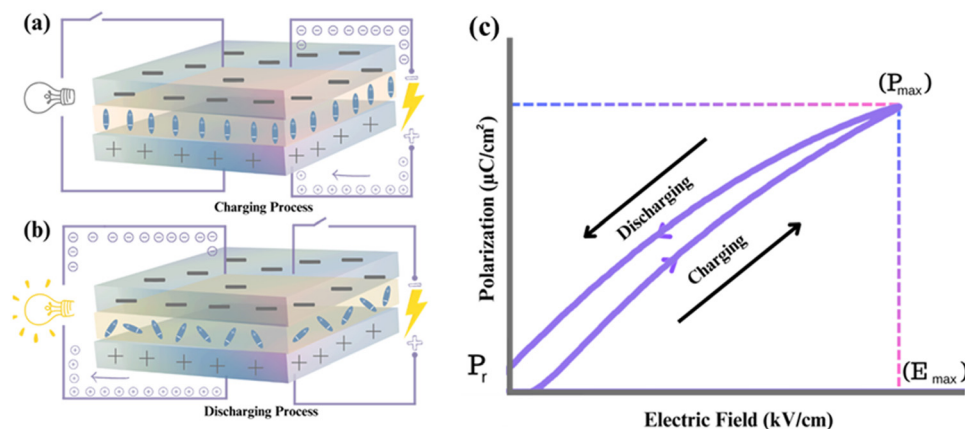


Fig. 4   (a) Charging process (b) discharging process (c) P–E loop of evaluating energy storage performance of the dielectric capacitors.

The energy storage of dielectric capacitors is related to capacitance ($C$), which is defined as the charge ($\mathrm{d}Q$) induced by an external electric field ($\mathrm{d}V$), as illustrated in Fig. 4c. The capacitance is calculated using the permittivity and geometry, as shown in eqn (1):

$$C = \frac{\mathrm{d}Q}{\mathrm{d}V} = \varepsilon_0 \varepsilon_r \frac{A}{t} \qquad (1)$$

where $\varepsilon_0$ is the permittivity of the vacuum, $\varepsilon_r$ is the relative permittivity, $t$ is the thickness of the dielectric medium, and $A$ is the area of the dielectric capacitors.

The energy storage density depends on $\varepsilon_r$ and the applied electric field for all dielectrics. Due to energy dissipation via Joule heat loss, particularly in nonlinear dielectrics, the recoverable energy storage density ($W_{rec}$) is used to quantify the energy that can be recovered during the discharge cycle. $W_{rec}$ is calculated as an integral of maximum polarisation ($P_{max}$) and remnant polarisation ($P_r$), as shown in eqn (2):

$$W_{rec} = \int_{P_r}^{P_{max}} E \mathrm{d}P \qquad (2)$$

10764 | Chem. Soc. Rev., 2024, 53, 10761–10790

This journal is © The Royal Society of Chemistry 2024

Achieving high energy density in dielectrics involves a combination of high $P_{max}$, low $P_r$, high breakdown strength, and low dielectric loss. Understanding and controlling these nonlinear effects is essential in various applications, as they may limit the $W_{rec}$. Moreover, energy efficiency ($\eta$) is an important indicator for dielectric capacitors, alongside $W_{rec}$, particularly in practical applications. Energy efficiency is expressed by eqn (3):

$$\eta = \frac{W_{rec}}{W_{rec} + W_{loss}} \qquad (3)$$

where $W_{loss}$ is the unrecoverable or lost energy density during discharging. High $\eta$ is desirable for practical applications, ideally exceeding 90%, to minimise self-heating during operation.

## 2.2. Polarisation

Polarisation–electric ($P$–$E$) loops, obtained from ferroelectric hysteresis measurements, demonstrate characteristics such as $P_{max}$ and $P_r$, coercive electric field ($E_c$), and $E_{max}$. These loops are typically obtained by measuring charge with a classical sawyer-tower circuit,[16] which provides a preliminary estimate of energy storage performance. In this context, it's important to note that the electric displacement–electric field ($D$–$E$) loops may maybe more theoretically accurate to evaluate the energy storage performance of a ceramic capacitor since $W_{rec}$ values are evaluated under the application of electric field. However, most of the studies assess their materials using $P$–$E$ instead of $D$–$E$ (based on ferroelectric hysteresis loops) because polarisation is closely related to the electric displacement based on the equation below:

$$D = \varepsilon_0 E + P \qquad (4)$$

where $\varepsilon_0$, $E$ and $P$ are the vacuum permittivity, applied electric field and polarisation.

Based on the form features of $P$–$E$ loops shown in Fig. 5, dielectrics are categorised into four specific groups: ferroelectric (FE), antiferroelectric (AFE), relaxor (RFE), and linear dielectric (LD).[17] FEs, as shown in Fig. 5(a), exhibit high $P_{max}$ and $P_r$, which collectively lead to nonlinear $P$–$E$ loops, resulting in low $E_{max}$ (less than 100 kV cm$^{-1}$), $W_{rec}$ and $\eta$, making them unsuitable for energy storage capacitor applications. AFEs, Fig. 5(b), exhibit dual hysteresis characteristics, with linear behaviour and FE loops positioned before and after, respectively, the critical switching field, making them desirable for energy storage applications. RFEs, obtained through the process of chemical doping, exhibit slim polarisation hysteresis loops as shown in Fig. 5(c), high $P_{max}$ and low $P_r$, ideal for high $W_{rec}$. LDs, in Fig. 5(d), on the other hand, typically exhibit low $P_{max}$ and $P_r$ due to their low $\varepsilon_r$ but can theoretically achieve high efficiency ($\eta > 90\%$). The low energy storage density due to low $P_{max}$ and $\varepsilon_r$ ensures a low volumetric efficiency for any device but linear dielectrics with higher values of $P_{max}$ and permittivity ($>500$) would constitute a breakthrough in dielectric technology.[18]



Fig. 5 Typical $P$–$E$ loops for (a) ferroelectrics – FE (b) antiferroelectrics – AFE (c) relaxor ferroelectrics – RFE (d) linear dielectrics – LD.

Delta polarisation, $\Delta P$ ($P_{max} - P_r$), is crucial for assessing the energy storage capabilities of dielectric materials and depends on many factors such as grain size, microstructure, core–shell morphology, and electrode area. Moreover, minimising $P_r$ is essential for efficient energy storage, allowing for effective energy release with minimal losses. These parameters can be optimised through material design, processing, and other strategies to enhance energy storage performance. Understanding and maximising $\Delta P$ are imperative for designing materials with favourable $P$–$E$ loop characteristics, ultimately enhancing energy storage performance.[18]

It is also critical to understand the origin of polarisation for the lead-free dielectric/ferroelectric ceramics since some ultra-high polarisation values ($> 50$ uC cm$^{-2}$, see Table 6 below) have been reported for dielectric thin films. It is impossible to get measured polarisation higher than spontaneous polarisation ($P_s$) which is a fixed value for a conventional ferroelectric (except the case for additional field-induced transition to produce higher $P_s$). $P_s$ of ferroelectric ceramic systems can be calculated based on neutron diffraction, as proposed by Shimakawa *et al.*[19] Then spontaneous polarisation caused by displacements can be calculated using Shima Kawa's model as follows:

$$P_s = \sum_i \frac{m_i \Delta x_i Q_i e}{V} \tag{5}$$

where $m_i$ is the site multiplicity, $\Delta x_i$ is the atomic displacement along the $a$-axis from the corresponding position in the tetragonal structure, $Q_i e$ is the ionic charge of the $i$th constitute ion, and $V$ is the volume of the unit cell. For example, the $P_s$ of NBT-based ceramics, $0.8NBT$–$0.2(Ba_{0.4}Sr_{0.6}TiO_3)$, has been reported using eqn 5 above, resulting in 4.5 μC cm$^{-2}$.[20] Therefore, there is an urgent required to investigate further the contribution of such high polarisation, either by intrinsic (*e.g.*, electric field-induced phase transition) or extrinsic effects.

### 2.3. Dielectric breakdown strength

Dielectric breakdown ($E_{BD}$) is an undesirable physical phenomenon where materials ionise, causing an electrical current to flow instantly through capacitors at excessive voltage. $E_{max}$ is the maximum electric field a material can withstand before breakdown, while the maximum applied electric field is the highest applied field for effective energy storage at which the material breaks. $E_{max}$ is influenced by internal factors (band gap, activation energy, electrical microstructure) and external factors (defects, porosity). The pulse electric field ($E_{pulse}$) refers to short-duration, high-intensity fields that materials can endure in AC-pulsed conditions without breaking down. Most of the studies assess the energy storage performance of their materials using an $E_{pulse}$ of 1 to 20 Hz (based on $P$–$E$ loops). Moreover, Yan's group proposed a new concept for assessing energy storage materials, termed recoverable energy storage intensity ($\rho$). This metric is defined as the $W_{rec}$ per unit electric field difference ($\Delta E$), where $\Delta E$ is the difference between the breakdown field and the starting electric field. This approach provides a refined method for evaluating the efficiency of energy storage materials under specific electric field conditions.[21]

Several mechanisms have been proposed to explain dielectric capacitor failure, including thermal runaway, electromechanical breakdown, electric puncture, and partial discharge. A wider band gap ($E_g$) or activation energy ($E_a$) is considered a good indicator of higher $E_{max}$ for dielectric materials. Chemical doping is an effective method for tailoring $E_{max}$ by manipulating the electrical microstructure. Additionally, the thickness of ceramic specimens influences $E_{max}$ during high-voltage electrical measurements (discussed later with respect to Fig. 19). Achieving high $E_{max}$ is essential for high $W_{rec}$ and reliable energy storage performance. Overall, a high-density, single-phase ceramic with high $E_{max}$, high resistivity and homogeneous electrical microstructure is ideal for delivering high-energy storage.

## 3. State-of-art lead-free dielectric ceramics for high energy density capacitors

State-of-the-art lead-free dielectric ceramics (bulk ceramics, multilayer ceramic capacitors, and ceramic thin films) are discussed along with how energy storage performance may be normalised to take into account the effect of thickness and electrode area.

### 3.1. Bulk ceramics

**3.1.1. NaNbO₃.** Sodium niobate (NaNbO₃, NN), a lead-free AFE,[22] undergoes a series of phase transitions upon heating as shown in Fig. 6.[23–27] Under the application of an electric field, the room-temperature AFE P phase is irreversibly transformed to the FE Q phase ($P2_1ma$), resulting in an FE-like square hysteresis loop with large polarisation values ($P_r$ = 30 μC cm$^{-2}$ at 150 kV cm$^{-1}$),[28,29] Fig. 6. The volume fraction of the P *vs.* Q phase in the unpoled state depends on many factors such as impurity concentration and grain size. NN has a comparatively large intrinsic band gap ($E_g \sim 3.58$ eV)[30] among lead-free perovskite dielectrics, thus it is considered a promising candidate for sustaining a high $E_{max}$[31,32] and therefore $W_{rec}$.

Recent studies on NN-based dielectric ceramics have been summarised in Table 1, which are primarily focused on (i) A-site chemical dopants (Na),[34] (ii) B-site chemical dopants (Sr, Sn, Zr, Hf, W, Mn),[35–37] (iii) A and B-site co-doping (Bi/Ta, Bi/Mg, Ca/Zr)[38–40] and (iv) formation binary (NN–CaHfO₃, CaTiO₃ (CT), BT, BiScO₃, SrTiO₃ (ST), AN, and CaZrO₃ (CZ))[41–45] and ternary solid solution.[22,33,35–37,40,45–54] NN-based systems have a dominant room temperature AFE structure with anti-parallel cation displacements normal to the long ($b$) axis.[25,55] The AFE phase has a similar free energy to the FE Q phase and transforms irreversibly to the latter on the application of an electric field.[25] However, the AFE structure may be stabilised using dopants that decrease the Goldschmidt perovskite (general
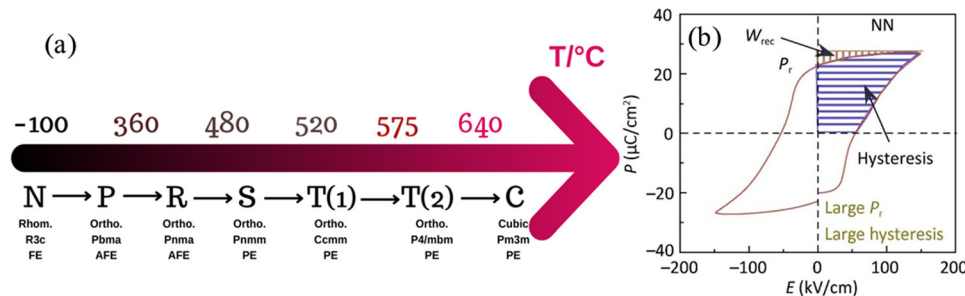
**10766** | *Chem. Soc. Rev.*, 2024, **53**, 10761–10790

This journal is © The Royal Society of Chemistry 2024

**Fig. 6** (a) Phase transition of NN ceramics as a function of temperature (b) PE Loop of NN.[33] Reprinted (adapted) with permission from ref. 33 under the terms of the Creative Commons CC BY license, Elsevier.

**Table 1** Summary of energy storage performance of NN-based ceramics from the literature

| Composition | $W_{rec}$ (J cm$^{-3}$) | $\eta$ (%) | $E$ (kV cm$^{-1}$) | $\Delta P$ ($\mu$C cm$^{-2}$) | $\tau_{0.9}$ (ns) | $P_D$ (MW cm$^{-3}$) | $\varepsilon_r$ (RT) | $\tan\delta$ (RT) | $t$ (mm) | Ref. |
|---|---|---|---|---|---|---|---|---|---|---|
| 0.69NN–0.06BT–0.25Ca$_{0.7}$La$_{0.2}$TiO$_3$ | 3.1 | 91 | 360 | 18 | — | 154 | 412 | 0.013 | 0.10 | 58 |
| 0.90(0.88NN–0.12Bi(Ni$_{0.5}$Zr$_{0.5}$)O$_3$)–0.10CT | 5.1 | 83 | 580 | 12 | 35 | 75 | 383 | 0.010 | 0.10 | 59 |
| 0.85NN–0.15CZ | 5.4 | 82 | 680 | 32 | — | — | 545 | — | 0.10 | 48 |
| 0.8(0.92NN–0.08Bi (Mg$_{0.5}$Ti$_{0.5}$)O$_3$)–0.2 CT | 5.7 | 86 | 475 | 31 | 28 | 48 | 373 | 0.003 | 0.10 | 31 |
| 0.96(0.8NN–0.2 ST)–0.04 Bi(Zn$_{0.5}$Sn$_{0.5}$)O$_3$ | 5.8 | 92 | 573 | 11 | — | — | 712 | 0.009 | 0.10 | 60 |
| 0.85(0.92NN–0.08 Bi(Mg$_{0.5}$Ti$_{0.5}$)O$_3$–0.15 ST | 6.0 | 81 | 590 | 19 | 990 | 96 | 620 | 0.002 | 0.15 | 51 |
| 0.84NN–0.16CT | 6.6 | 93 | 520 | 15 | 700 | 350 | 730 | 0.009 | 0.10 | 42 |
| Na$_{0.9}$Bi$_{0.1}$Nb$_{0.9}$Ta$_{0.1}$O$_3$ | 7.3 | 87 | 530 | 30 | 60 | 320 | 1450 | 0.002 | 0.15 | 38 |
| 0.75[0.90NN–0.10Bi(Mg$_{0.5}$Ta$_{0.5}$)O$_3$]–0.25(Bi$_{0.5}$Na$_{0.5}$)$_{0.7}$Sr$_{0.3}$TiO$_3$ | 8.0 | 90 | 800 | 23 | 32 | 49 | 620 | 0.005 | 0.15 | 61 |
| 0.88NNTa$_{0.1}$–0.10ST–0.02La(Mg,Ti)O$_3$ | 8.7 | 80 | 580 | 37 | — | — | 515 | 0.008 | 0.20 | 18 |
| 0.85 NN–0.15 Ca$_{0.7}$Sm$_{0.2}$TiO$_3$ | 9.1 | 80 | 800 | 31 | 80 | 157 | 605 | 0.007 | 0.035 | 62 |
| (Na$_{0.91}$Bi$_{0.09}$)(Nb$_{0.94}$Mg$_{0.06}$)O$_3$ | 10.9 | 83 | 820 | 30 | 19 | — | 920 | 0.002 | 0.06–0.08 | 63 |
| 0.76NN–0.24(Bi$_{0.5}$N$_{0.5}$) TiO$_3$ | 12.2 | 69 | 620 | 59 | — | — | 1320 | — | 0.15 | 64 |
| 0.88 NN–0.12(Bi$_{0.9}$Na$_{0.1}$)(Fe$_{0.8}$Ti$_{0.2}$) O$_3$ | 12.7 | 83 | 873 | 27 | 5000 | 200 | 650 | 0.002 | 0.05 | 65 |
| 0.88 NN–0.12(0.7BF–0.3BT) | 14.5 | 84 | 930 | 55 | 4500 | 233 | 780 | 0.002 | 0.05 | 66 |
| 0.12 NN–0.12(0.55BF–0.45 ST) | 16.2 | 82 | 970 | 61 | 4800 | 178 | 910 | 0.004 | 0.05 | 55 |

formula, ABO$_3$) tolerance factor, $t$.[56]

$$t = \frac{r_A + r_O}{\sqrt{2}(r_B + r_O)} \qquad (6)$$

where $r_A$, $r_B$ and $r_O$ are the ionic radii of the A-, B-, and O-sites, respectively. Besides $t$, the average electronegativity (X) difference between the ions also plays a role, where $X_{BO}$ is the electronegativity difference between the B cation and the oxygen anion while $X_{AO}$ is the electronegativity difference between the A cation and the oxygen anion, respectively,[57]

$$\Delta X = \frac{X_{BO} + X_{AO}}{2} \qquad (7)$$

For example, $t$ for the conventional lead-based AFE PbZrO$_3$ is 0.964, lower than NN with a similar $\Delta X$ of 2.25 to ST and BT. Thus, NN's AFE may be stabilised by lowering its t value while holding $\Delta X$ constant.[57] Recently, FE Q phase NN was stabilised in 0.9NN–0.1ST, which is further modified to a short-range relaxor 0.88NN–0.10ST–0.02La(Mg, Ti)O$_3$ and then to an incipient/paraelectric for 0.88NaNb$_{0.9}$Ta$_{0.1}$O$_3$–0.10ST–0.02La(Mg, Ti)O$_3$ that exhibits quasi-linear dielectric (QLD) behaviour, where $\tan\delta$ remained <0.01 between −143 to 290 °C (130 to

563 K) for NNTa$_{0.10}$–10ST–2LMT (Fig. 7a). The polarisation increment, d$P$/d$E$, for QLD was found to be near constant (0.008 $\mu$C cm$^{-1}$ kV$^{-1}$) up to $E$ > 500 kV cm$^{-1}$, giving rise to excellent $W_{rec}$ = 8.7 J cm$^{-3}$ with $\eta$ = 80% (Fig. 7b–d).[18] To date, a 50 $\mu$m-thick 0.88NN–0.12(0.55BF–0.45ST) ceramic has been reported with the highest $W_{rec}$ ∼16.2 J cm$^{-3}$ with $\eta$ ∼82%.

**3.1.2. AgNbO$_3$.** AgNbO$_3$ (AN) has emerged as a promising candidate, demonstrating substantial potential for energy storage due to its high polarisation, 52 $\mu$C cm$^{-2}$.[67] In the ideal cases, the $P_r$ value of AFE materials is zero, but undoped AFE AN co-exists with a ferrielectric AFE/FE phase resulting in non-zero $P_r$ (∼7 $\mu$C cm$^{-2}$) and low $E_{max}$ at room temperature.[68] There are three principal strategies to enhance the energy density of AN-based ceramics.[29] The first entails the incorporation of MnO$_2$, a technique inspired by lead-based materials, to mitigate leakage current.[68,69] In addition to pinning V$_O$ and inhibiting their movement, MnO$_2$ refines the grain size which also decreases electrical conductivity, resulting from the refractory nature of the dopants and the elevated sintering temperatures needed for doped AN ceramic, advantageous for achieving higher $E_{max}$.[70] The second strategy, the most widely adopted, involves aliovalent doping at the A-site and replacing Nb with Ta.[69,71–75] Notably, the substitution of Nb with Ta has garnered

**Fig. 7** (a) Temperature-coefficient of capacitance (TCC) values of NNTa$_{0.10}$–10ST–2LMT across the temperature range from 800 K, (b) temperature-dependent $M''$ spectroscopic plots for NNTa$_{0.10}$–10ST–2LMT, (c) $P$–$E$ loops of NNTa$_{0.10}$–10ST–2LMT bulk ceramics, and (d) Calculated discharge energy density ($U$) and energy conversion efficiency ($\eta$) at various electric fields.[18] Reprinted with permission from ref. 18, the John Wiley and Sons., under the terms of the Creative Commons CC BY license.

considerable attention in recent AN-based research. Ta is known to stabilise the AFE phase by regulating the M2 or M3 transitions, evident from the shift in temperature of the dielectric anomalies and disruption of long-range antipolar AFE order which reduces the scale of AFE domains. Ultimately for the AgTaO$_3$ end member, an incipient FE response is observed.[76] Before the onset of incipient behaviour, the field required to promote the AFE/FE transition is increased. Within the field-induced FE phase, polar coupling is also reduced, and the loop is slimmer, simultaneously increasing $\eta$ and $W_{rec}$. A-site substitutions with RE and Bi ions enhance this effect due to the difference in ionic radius with Ag which also affects the correlation length of antipolar order in the AFE and polar coupling in the induced FE phase.[77,78] Therefore, to enhance

energy storage properties, AN-based materials sacrifice $P_{max}$, leading to an increase in $E_g$ and $E_a$, thus contributing to higher $\eta$, lower strain, and enhanced $E_{max}$, ultimately leading to higher $W_{rec}$.

The third strategy involves the formation of a solid solution with other compounds, such as (Sr$_{0.7}$Bi$_{0.2}$)HfO$_3$ and Ca(Hf$_{0.2}$Ti$_{0.8}$)O$_3$[79,80] to induce relaxor rather than AFE/FE switching behaviour. Recently, a significant milestone has been the successful development of AN-based MLCCs by several research groups,[71,72] which have achieved high $W_{rec}$, principally due to a reduction in thickness of the dielectric layer in relaxor-based systems (third strategy). Fig. 8 shows a TEM image of Ag$_{0.64}$Bi$_{0.12}$NbO$_3$ + 0.10 wt% MnO$_2$ revealing lamellar domains, with Fig. 8b demonstrating the highest $W_{rec}$ to date
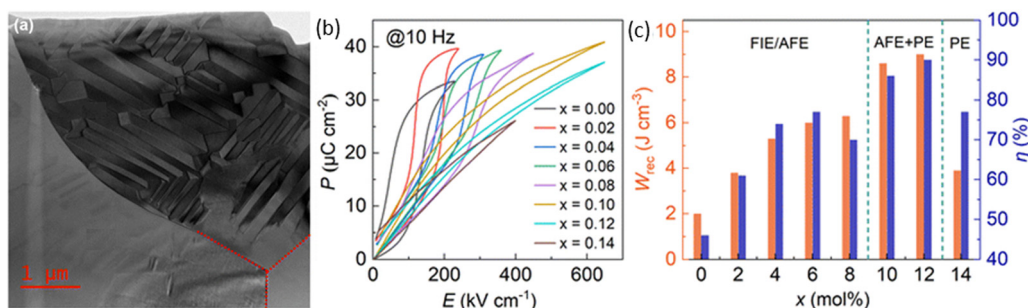


**Fig. 8** (a) Overview of bright-field TEM image displaying three grains of the Ag$_{0.64}$Bi$_{0.12}$NbO$_3$ + 0.10 wt% MnO$_2$ ceramic (b) unipolar $P$–$E$ loops measured at 10 Hz, and (c) $W_{rec}$ and $\eta$ of AN–$x$Bi ceramics at room temperature.[77] Reproduced from ref. 77 with permission from the Royal Society of Chemistry.

**10768** | *Chem. Soc. Rev.*, 2024, **53**, 10761–10790

This journal is © The Royal Society of Chemistry 2024

**Table 2** Functional properties of the AN-based Ceramics from the literature

| Composition | $W_{rec}$ (J cm$^{-3}$) | $\eta$ (%) | $E$ (kV cm$^{-1}$) | $\Delta P$ ($\mu$C cm$^{-2}$) | $\tau_{0.9}$ (ns) | $P_D$ (MW cm$^{-3}$) | $\varepsilon_r$ (RT) | tan $\delta$ (RT) | $t$ (mm) | Ref. |
|---|---|---|---|---|---|---|---|---|---|---|
| $Ag_{0.99}Nd_{0.01}Nb_{0.796}Ta_{0.2}O_3$ | 4.5 | 68 | 290 | 36 | — | — | 520 | 0.030 | — | 81 |
| 0.94 AN–0.06 $CaHf_{0.2}Ti_{0.8}O_3$ + 0.2wt% Mn | 5.4 | 66 | 300 | 38 | — | — | 400 | 0.003 | — | 80 |
| $Ag_{0.92}Sr_{0.04}Nb_{0.78}Ta_{0.22}O_3$ | 5.6 | 70 | 300 | 36 | 137 | 132 | 600 | 0.007 | — | 82 |
| $Ag_{0.80}Na_{0.20}Nb_{0.80}Ta_{0.20}O_3$+ 0.1% $MnO_2$ | 5.8 | 62 | 260 | 46 | 160 | — | 431 | 0.005 | 0.08 | 73 |
| AN@$SiO_2$ + 0.10 wt% $MnO_2$-doped + 4 mol% $Bi_2O_3$ and $Sc_2O_3$ | 5.9 | 71 | 322 | 42 | 160 | 273 | 813 | 0.001 | 0.06 | 83 |
| 0.945AN–0.055$Sr_{0.7}Bi_{0.2}HfO_3$ + 1 mol% $BaCu(B_2O_5)$ | 6.1 | 73 | 330 | 40 | — | — | 600 | 0.002 | 0.15 | 79 |
| $Ag_{0.94}La_{0.02}Nb_{0.8}Ta_{0.2}O_3$ | 6.7 | 74 | 540 | 33 | — | — | 550 | — | 0.12 | 84 |
| $Ag_{0.76}La_{0.08}NbO_3$ | 7.0 | 77 | 476 | 35 | — | — | 660 | 0.003 | 0.15 | 78 |
| $Ag_{0.96}Ce_{0.01}Nb_{0.7}Ta_{0.3}O_3$ | 7.4 | 76 | 377 | 41 | 23 | 294 | 580 | — | 0.13 | 85 |
| 0.90AN–0.10$Bi_{0.2}Sr_{0.7}TiO_3$ | 7.8 | 56 | 580 | 45 | 310 | — | 950 | 0.180 | 0.05 | 69 |
| $Ag_{0.80}Bi_{0.04}Sr_{0.04}NbO_3$ + 0.1 wt%$MnO_2$ | 7.9 | 75 | 702 | 37 | — | — | 844 | 0.009 | 0.05 | 70 |
| $Ag_{0.80}Bi_{0.04}Sr_{0.04}Nb_{0.85}Ta_{0.15}O_3$ + 0.30 wt% $MnO_2$ | 8.5 | 76 | 729 | 33 | 300 | — | 687 | 0.003 | 0.05 | 74 |
| $Ag_{0.64}Bi_{0.12}NbO_3$ + 0.10 wt%$MnO_2$ | 9.0 | 90 | 651 | 39 | — | — | 1100 | — | 0.05 | 77 |

for AN-based materials.[77] The energy storage properties of AN-based materials are summarised in Table 2.

**3.1.3. $Na_{0.5}Bi_{0.5}TiO_3$.** $Na_{0.5}Bi_{0.5}TiO_3$ (NBT) is one of the most studied lead-free electroceramics. The properties of modified compositions include large electro-strain,[86] oxygen ion conduction,[87] and large electrostatic energy storage.[29,63,88,89] Undoped NBT exhibits a FE $P$–$E$ loop with $P_{max} \sim 40 \mu$C cm$^{-2}$,[90] $P_r \sim 38 \mu$C cm$^{-3}$ and $E_c$ of 73 kV cm$^{-1}$.[91] NBT was thought to have an average rhombohedral $R3c$ structure but more recent studies have identified the room temperature phase as monoclinic with $Cc$ symmetry,[87,92] as reported by Jones.[93] For high-field applications, the leakage in undoped NBT is caused by defects relating to $Bi^{3+}$ volatilisation[94,95] during calcination and densification, however, excess $Bi_2O_3$ to the stoichiometric composition improves the total resistivity. Early studies focused on A, B or A/B site (co-) doping, promoting relaxor behaviour, such as Na, Bi, Sr, or Ba on A-site[96–116] or Nb, Mg, Fe, Mn, or Ti on B-site[96,115–123] sites, and Na/Nb, Ba/Mg, Bi/Na, and Sr/Mg, Nb co-doped[29,92,124–157] yielding $W_{rec}$ up to 4 J cm$^{-3}$ for bulk ceramics.

As with AN, there are several strategies employed to optimise energy density in NBT-based ceramics. NBT is often combined with end members that have a large $E_g$, such as ST, $Sr_{0.7}Bi_{0.2}TiO_3$ (SBT) and $Ca_{0.7}La_{0.2}TiO_3$[158] to form a relaxor phase (pseudo-cubic) with polar nano regions (PNRs). A high $W_{rec}$ $\sim$10.3 J cm$^{-3}$ with $\eta \sim$97%[159] was reported by Zhou et al., in 0.85 $(Bi_{0.5}Na_{0.5})_{0.7}Sr_{0.3}TiO_3$ (BNST)–0.15 $Bi(Mg_{1/3}Ta_{2/3})O_3$ (BMT) in which $Sr^{2+}$, Mg and Ta ions promote the formation of PNRs, due to their larger ionic radius leading to lattice strain which not only disrupts polar coupling (Fig. 9)[160] but locally enhances polarisation.[161] The low tolerance factor associated with NBT-based ceramics ensures that not only is their chemical and displacive cation disorder but also of the $O^{-2}$ octahedral framework in which the amplitude and type of rotation (in-phase vs. antiphase) varies over a short range. Liu and co-authors[162] utilised these strategies albeit expressed in different terms and reported 0.88 (0.75 NBT–0.25BT)–0.12NN ceramics with $W_{rec} \sim$ 15.2 J cm$^{-3}$, $\eta \sim$91%, $E_{max} \sim$730 kV cm$^{-1}$, $\tau_{0.9} \sim$38 ns, temperature stability from 30–120 °C, frequency stability form 10–200 Hz and cyclic fatigue resistance (up to 10$^7$ cycles, with less than 1% changes).[162] Energy density performance for a

wide range of NBT-based compositions is summarised in Table 3.

**3.1.4. $BiFeO_3$.** Bismuth ferrite, $BiFeO_3$ (BF)-based lead-free ceramics are considered promising candidates for high energy density capacitors due to the large spontaneous polarisation and high Curie temperature ($T_c$) of the $BiFeO_3$ end member.[172,173] $Bi^{3+}$ has a similar electronic configuration to $Pb^{2+}$ with a lone electron pair contributing to higher $T_c$.[174] BF is both an antiferromagnetic and FE material at room temperature (RT) which has attracted attention in the field of multiferroics.[175] However, the properties of undoped BF generally are very poor, with large leakage current, high tan $\delta$, and low $W_{rec}$. Most research has adopted chemical dopants to overcome these issues which arise mainly due to the multiple and unstable valence of the Fe ions coupled with Bi volatilisation during processing.[176] Therefore, BF-based dielectric ceramics are modified by doping at A- and/or B-site e.g. Nd,[177] alloying with a third compound e.g. $Bi(Zn_{2/3}Nb_{1/3})$[178] or both, e.g. 0.61BF–0.33$(Ba_{0.8}Sr_{0.2})$ $TiO_3$–0.06La $(Mg_{2/3}Nb_{1/3})O_3$ to improve electrical properties.[179] The BF–BT solid solution was the first solid solution to exhibit large $W_{rec}$[177,180,181] but the highest (16.3 J cm$^{-3}$) with $\eta \sim$ 86% at $E_{max} \sim$690 kV cm$^{-1}$ was reported for a 50 μm-thick 0.62$Bi_{0.9}La_{0.1}FeO_3$ (BLF)–0.3$Ba_{0.7}Sr_{0.3}TiO_3$ (BST)–0.08 $K_{0.5}Na_{0.5}NbO_3$ (KNN) bulk ceramic,[182] Fig. 10a. Other BF-based binary solid solutions include BF–$K_{0.5}Bi_{0.5}TiO_3$ (BF–KBT)[183] and BF–ST[184] and are summarised in Table 4. Wang and co-authors[183] reported a 0.5KBT–0.42BF–0.08$Sm(Mg_{2/3}Nb_{1/3})O_3$ (SMN) ceramics with the formation of lamellar nanodomains (Fig. 10b), giving $W_{rec} \sim$ 6.1 J cm$^{-3}$ with $\eta$ of 72% at $E$ = 410 kV cm$^{-1}$,[183] along with good temperature stability from 25 to 150 °C (<15% variation). 0.35BF–0.65ST ceramics have also been reported with $W_{rec}$ = 8.4 J cm$^{-3}$ with $\eta \sim$ 90% at $E_{max}$ = 750 kV cm$^{-1}$ after a two-step sintering method (TSSM) which improved grain size, $E_{max}$, and $W_{rec}$, with less than 10% variation from 1–100 Hz and from 10–120 °C when compared to one-step sintering methods (OSSM), Fig. 10(c and d).[184]

One of the key factors to improve $E_{max}$ and $W_{rec}$ in BF-based dielectrics is the optimisation of the electrical microstructure, as proposed by Wang et al.[181] For example, adding a third
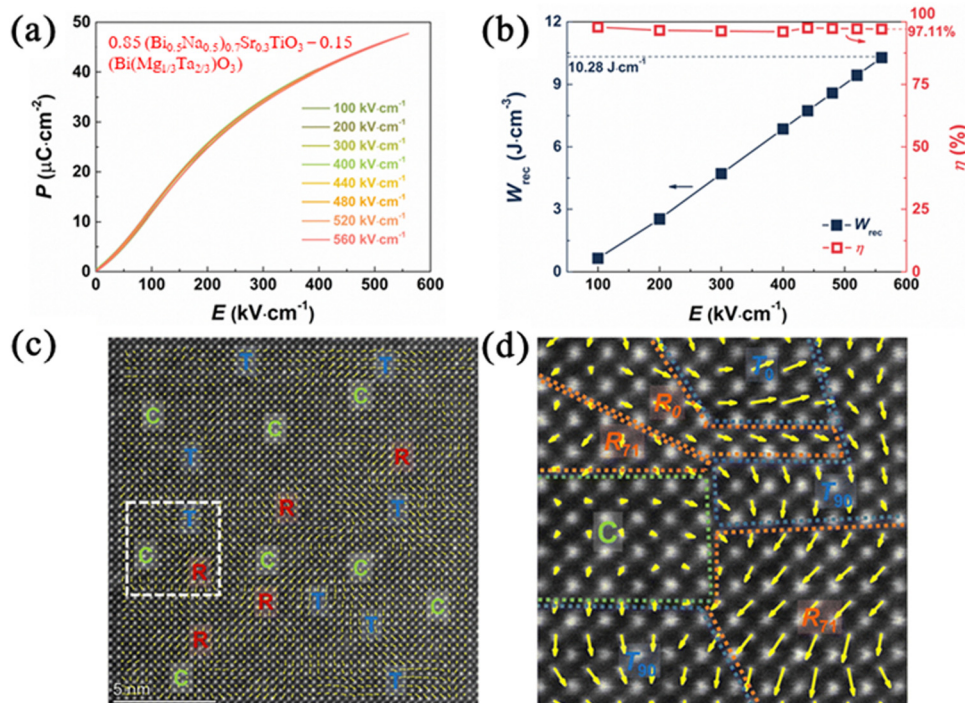
This journal is © The Royal Society of Chemistry 2024

Chem. Soc. Rev., 2024, **53**, 10761–10790 | **10769**

**Fig. 9** Properties of 0.85 $(Bi_{0.5}Na_{0.5})_{0.7}Sr_{0.3}TiO_3$–0.15 $(Bi (Mg_{1/3}Ta_{2/3}) O_3)$ ceramics (a) $P–E$ Loops (b) $W_{rec}$ and $\eta$ values (c) HRDP STEM polarisation vector image along $[100]_c$ (d) enlarged image from the white frame.[160] Reproduced from ref. 160 with permission from the Royal Society of Chemistry.

**Table 3** Functional properties of the NBT-based Ceramics from the literature

| Composition | $W_{rec}$ (J cm$^{-3}$) | $\eta$ (%) | $E$ (kV cm$^{-1}$) | $\Delta P$ ($\mu$C cm$^{-2}$) | $\tau_{0.9}$ (ns) | $P_D$ (MW/cm$^3$) | $\varepsilon_r$ at RT | tan($\delta$) at RT | $t$ (mm) | Ref. |
|---|---|---|---|---|---|---|---|---|---|---|
| 0.465NBT–0.035CaSnO$_3$–0.5Sr$_{0.7}$B$_{0.2}$TiO$_3$ | 4.0 | 80 | 415 | 38 | 116 | 107 | 2600 | 0.013 | 0.15 | 163 |
| 0.94Bi$_{0.4867}$Sm$_{0.0133}$Na$_{0.4601}$Sm$_{0.0133}$TiO$_3$–0.06BaTiO$_3$ | 4.4 | 84 | 230 | 42 | — | — | 990 | 0.035 | 0.11 | 21 |
| 0.75 NBT–0.25(Bi(Mg$_{0.5}$Hf$_{0.5}$Mg$_{0.5}$Hf$_{0.5}$)O$_3$) | 4.6 | 75 | 310 | 21 | 110 | 39.1 | 430 | 0.023 | 0.12 | 164 |
| 0.62NBT–0.3Sr$_{0.7}$Bi$_{0.2}$TiO$_3$–0.08BiMg$_{2/3}$Nb$_{1/3}$O$_3$ | 7.5 | 92 | 470 | 48 | — | — | 1230 | 0.061 | 0.15 | 89 |
| 0.85(0.94NBT–0.06BT)–0.15 BiMg$_{0.5}$Hf$_{0.5}$O$_3$ | 7.8 | 76 | 370 | 35 | — | — | 1600 | 0.230 | 0.20 | 90 |
| 0.85 Bi$_{0.47}$Na$_{0.47}$Ba$_{0.06}$TiO$_3$–0.15 Sr(Al$_{0.5}$Ta$_{0.5}$) O$_3$ | 8.3 | 91 | 555 | 39 | 97 | — | 1460 | — | 0.05 | 165 |
| 0.90(Bi$_{0.5}$Na$_{0.5}$) 0.65 Sr$_{0.35}$TiO$_3$–0.10 Bi(Mg$_{0.5}$Zr$_{0.5}$) O$_3$ | 8.5 | 86 | 522 | 59 | — | — | 1320 | 0.165 | 0.10 | 166 |
| 0.92(0.6NBT–0.4Sr$_{0.7}$Bi$_{0.2}$TiO$_3$)–0.08 BMT | 8.6 | 93 | 565 | 45 | — | — | 1350 | 0.090 | 0.60 | 167 |
| NBT–Bi$_{0.5}$K$_{0.5}$TiO$_3$–Sr (Sc$_{0.5}$Nb$_{0.5}$) O$_3$ | 9.2 | 96 | 385 | 46 | 244 | — | 750 | 0.014 | 0.05 | 168 |
| 0.76(0.94NBT–0.06BT)–0.24 CaTi$_{0.75}$Ta$_{0.2}$O$_3$ | 9.6 | 88 | 410 | 60 | — | 117 | 789 | 0.020 | 0.11 | 169 |
| 0.85 BNST–0.15 BMT | 10.3 | 97 | 420 | 54 | 1350 | — | 615 | 0.045 | 0.05 | 159 |
| 0.50(0.75NBT–0.25BT)–0.50 BaZrO$_3$ | 13.6 | 91 | 660 | 63 | 35 | 313 | 455 | 0.070 | 0.08 | 170 |
| (Bi$_{0.5}$Na$_{0.5}$)(Ti$_{0.33}$Fe$_{0.33}$Nb$_{0.33}$) O$_3$ | 13.8 | 82 | 640 | 53 | 35 | 136 | 480 | 0.019 | 0.05 | 171 |
| 0.62(0.94NBT–0.06BT)–0.38 Ca$_{0.7}$La$_{0.2}$TiO$_3$ | 15.1 | 82 | 640 | 61 | 32 | 212 | 710 | 0.001 | 0.12 | 158 |
| 0.88(0.75 NBT–0.25BT)–0.12 NN | 15.2 | 91 | 730 | 30 | 38 | — | 1896 | 0.003 | 0.05 | 162 |

compound SMN into BF–KBT resulted in lower conductivity, higher $E_a$ and electrical homogeneity,[183] favouring high $E_{max}$ as well as $W_{rec}$. In impedance complex plots such as Fig. 11(a), there are two $M''$ ($M'' = 1/2C$ where $C$ is capacitance) peaks at each temperature, indicating heterogeneous electrical microstructure (two-component) of the undoped BF-KBT ceramic. Instead, only one $M''$ peak was identified for BF–KBT–0.08SMN ceramics, as shown in Fig. 11(b), whereas Fig. 11(c and d) shows the overlap of the $Z''$ over $M''$. Another example, 0.6BF–0.4ST–0.08BiMg$_{2/3}$Nb$_{1/3}$O$_3$ (BMN)–0.01Nb ceramics, as reported by Lu and co-authors,[192] also demonstrates that achieving electrical

homogeneity even at the weak field with a highly resistive and large $E_a$ is key to achieving high $E_{max}$ as well as $W_{rec}$.

### 3.2. Multilayer ceramic capacitors (MLCCs)

MLCCs are composed of co-fired multiple layers of ceramic and internal electrodes. The fabrication involves slurry preparation, tape-casting, screen printing, lamination, co-sintering and termination, Fig. 12.[194] By 2022, the market of ceramics MLCCs was ~10.9 billion USD and is expected to be ~16.77 billion by 2030.[195] There are different demands for MLCCs as they are used in many different areas of electronics such as electric
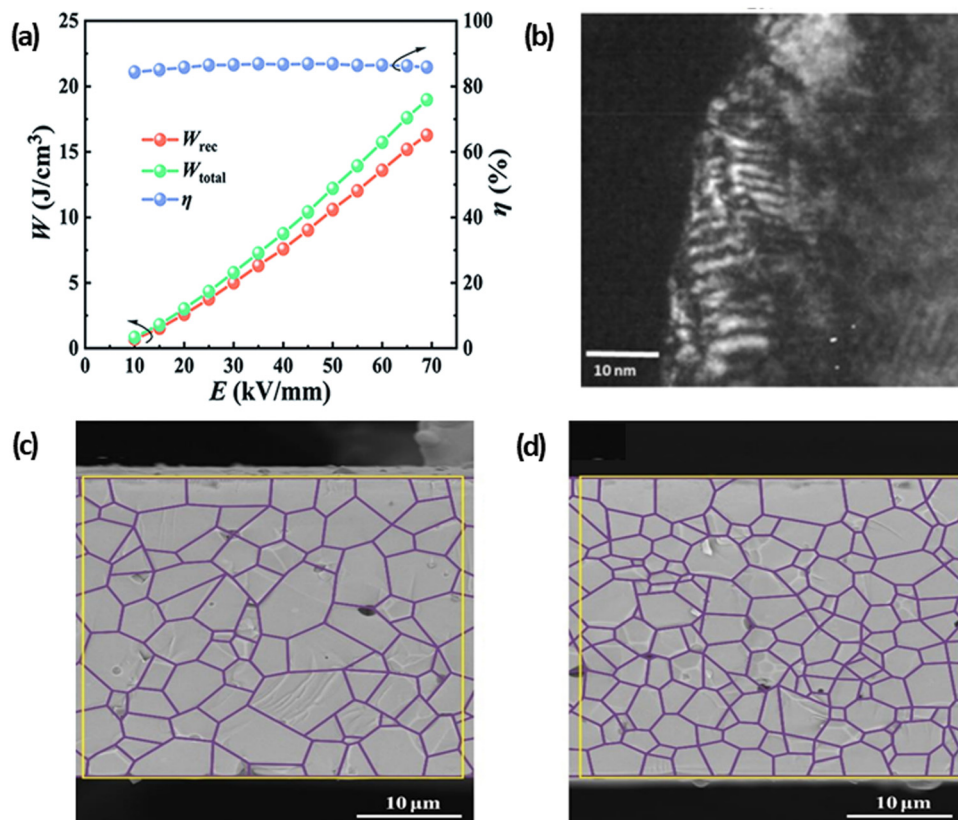
**10770** | Chem. Soc. Rev., 2024, **53**, 10761–10790

This journal is © The Royal Society of Chemistry 2024

Fig. 10    (a) $W_{rec}$ and $\eta$ values of 0.62 BLF–0.3 BST–0.08 KNN ceramics[182] (b) TEM image of grain with lamellar nanodomains for 0.5 KBT–0.42 BF–0.08 SMN.[183] SEM images for (c) OSSM and (d) TSSM 0.35BF–0.65ST ceramics.[184] Reproduced with permission ref. 182 from the Royal Society of Chemistry. Reprinted with permission ref. 183 from Elsevier under the terms of the Creative Commons CC-BY license. Reprinted with permission from ref. 184, the John Wiley and Sons.

Table 4    Functional properties of BF-based ceramics from the literature

| Composition | $W_{rec}$ (J cm$^{-3}$) | $\eta$ (%) | $E$ (kV cm$^{-1}$) | $\Delta P$ ($\mu$C cm$^{-2}$) | $\tau_{0.9}$ (ns) | $P_D$ (MW cm$^{-3}$) | $\varepsilon_r$ at RT | $\tan(\delta)$ at RT | $t$ (mm) | Ref. |
|---|---|---|---|---|---|---|---|---|---|---|
| 0.65BF–0.3 BT–0.05Bi (Zn$_{2/3}$Nb$_{1/3}$) O$_3$ + 0.1 wt% Mn$_2$O$_3$ | 2.1 | 53 | 180 | 33 | 100 | — | 450 | 0.010 | — | 178 |
| 0.56BF–0.30BT–0.14AN + 5% mol CuO | 2.1 | 84 | 195 | 26 | — | — | 620 | 0.020 | 0.30 | 185 |
| 0.7(Bi$_{0.97}$Nd$_{0.03}$) [Fe$_{0.95}$(Li$_{0.5}$Nb$_{0.5}$)$_{0.05}$] O$_3$–0.3BT + 0.1 wt% MnO$_2$ | 3.2 | 74 | 290 | 28 | — | — | 500 | — | — | 186 |
| 0.61BF–0.33(Ba$_{0.8}$Sr$_{0.2}$)TiO$_3$–0.06La(Mg$_{2/3}$Nb$_{1/3}$)O$_3$ + 0.1 wt% MnO$_2$ + 2 wt% BaCu(B$_2$O$_5$) | 3.4 | 59 | 230 | 27 | — | — | 380 | — | 0.30 | 187 |
| 0.5Bi$_{1.02}$FeO$_3$–0.37BT–0.13Bi(Zn$_{2/3}$(Nb$_{0.85}$Ta$_{0.15}$)$_{1/3}$)O$_3$ | 4.8 | 80 | 410 | 25 | — | — | 125 | — | 0.08 | 188 |
| 0.88(0.67BF–0.33BT)–0.12Na$_{0.73}$Bi$_{0.09}$NbO$_3$ | 5.6 | 84 | 410 | 14 | — | — | 700 | 0.090 | — | 189 |
| 0.5 KBT–0.42BF–0.08 SMN | 6.1 | 72 | 410 | 15 | — | — | 500 | 0.100 | 0.20 | 183 |
| 0.35BF–0.65ST | 7.5 | 93 | 626 | 33 | 166 | 280 | 430 | — | 0.04 | 184 |
| 0.85(0.7BF–0.3BT)–0.15NN | 8.2 | 70 | 275 | 65 | — | — | 1000 | — | 0.10 | 190,191 |
| 0.5BF–0.4 ST–0.03Nb–0.1BMN | 8.2 | 74 | 460 | 49 | — | — | 485 | — | 0.15 | 192 |
| 0.55BF–0.33BT–0.12NaTaO$_3$ | 13.4 | 90 | 580 | 62 | 6 | 158 | 750 | — | 0.05 | 176 |
| 0.62 BLF–0.3 BST–0.08 NaNb$_{0.85}$Ta$_{0.15}$O$_3$ | 15.9 | 88 | 680 | 57 | 6 | 192 | 590 | — | 0.05 | 193 |
| 0.62 BLF–0.3 BST–0.08 KNN | 16.3 | 86 | 690 | 64 | 6 | 181 | 550 | — | 0.05 | 182 |

vehicles, medical implants, servers, robotics, and bypass capacitors.[196,197] The leading companies for fabricating MLCCs include Murata Manufacturing and TDK Taiyo Yuden. The energy density performance of MLCCs is summarised in Table 5.

Lead-free RFE-type MLCCs have been reported in the literature with promising energy storage performance and reliability,

Table 5. For example, Lu and co-authors reported a 0.5BF–0.4 ST–0.03Nb–0.1BMN MLCC[192] with high $W_{rec}$ of 15.8 J cm$^{-3}$ with $\eta$ = 75.2% under $E_{max}$ ∼1000 kV cm$^{-1}$, as shown in Fig. 13. Nb$^{5+}$ donor doping was used to enhance resistivity with a third end-member (BMN) promoting relaxor behaviour.

More recently, the energy storage performance (evaluated from $P$–$E$ measurements) of the QLD MLCCs,

This journal is © The Royal Society of Chemistry 2024

*Chem. Soc. Rev.*, 2024, **53**, 10761–10790 | **10771**

**Fig. 11** Temperature-dependent $M''$ spectroscopic plots for KBT–BF–$x$SMN ceramics[183] (a) $x = 0.00$ and (b) $x = 0.08$. (c) $Z''$ and $M''$ spectroscopic plot for 0.6BF–0.4 ST ceramics at RT (d) $Z''$ and $M''$ spectroscopic plot for 0.6BF–0.4 ST–0.01Nb ceramics at 703 K.[192] Reprinted (adapted) with permission from ref. 183 under the terms of the Creative Commons CC BY license, Elsevier. Reprinted (adapted) with permission from ref. 192 under the terms of the Creative Commons Attribution 3.0 Unsupported Licence, Royal Society of Chemistry.

$0.88NaNb_{0.90}Ta_{0.10}O_3$ (NNT)–$0.10ST$–$0.02La(Mg, Ti)O_3$ (LMT), was $W_{rec} = 43.5$ ($\pm$ 2.6) J cm$^{-3}$ with $\eta = 85$ ($\pm$ 3) %, Fig. 14, at least twice that of all reported MLCCs to date.[18] The ultrahigh $W_{rec}$ obtained in the QLD type MLCCs not only depends on its ability to withstand high $E_{max}$ (associated with homogenous physical and electrical microstructure), low leakage conductivity and high activation energy) but also the QLD behaviour in which d$P$/d$E$ is constant of 0.0013 ($\pm$0.0002) $\mu$C cm$^{-1}$ kV$^{-1}$ from low-field (750 kV cm$^{-1}$) to high-field (2800 kV cm$^{-1}$). The origin of near constant d$P$/d$E$ still requires further investigation but is highly likely to be associated with weakly coupled polar displacements with random polarisation vectors (Fig. 14d).

Additionally, NBT-based MLCCs have demonstrated significant improvements in energy storage performance. For instance, ⟨111⟩-textured NBT–$Sr_{0.7}Bi_{0.2}TiO_3$ (NBT–SBT) multi-layer ceramics (discussed in section 4.4) achieved a remarkable $W_{rec}$ of 21.5 J cm$^{-3}$ with $\eta \sim 80\%$ at $E_{max} \sim 103$ MV m$^{-1}$. This enhancement in performance is attributed to the controlled grain orientation, which reduces the strain induced by the $E$ and improves $E_{max}$.[205] Priya and co-authors investigated AFE-type MLCCs with $Ag(Nb_{0.85}Ta_{0.15})O_3$ + 0.25 wt.% $MnO_2$ (ANT + Mn) as the dielectric.[81] The AFE-FE transition was observed

around 250 kV cm$^{-1}$, resulting in a decrease in $\eta$ from over 95% to approximately 70% (Fig. 15). These MLCCs exhibited a $W_{rec}$ of 7.9 J cm$^{-3}$ with $\eta$ measured at 71% at $E_{max} \sim 1020$ kV cm$^{-1}$, demonstrating lower performance compared to other lead-free REF-type MLCCs.

### 3.3. Ceramic thin films

Substantial progress in the development of lead-free thin films, *e.g.*, BT, NBT and BF, has been achieved through various synthesis methods, such as sputtering, pulsed laser deposition and chemical solution deposition[206–208] allowing precise control over composition and thickness.[209–215] Although thin films may have applications in electrostatic energy storage devices for highly miniaturised electronics requiring high voltage and high temperature, the technology cannot compete on cost with powder-based MLCC fabrication technology.

For dielectric thin films, both $E_{max}$ ($>2000$ kV cm$^{-1}$) and $W_{rec}$ ($>40$ J cm$^{-3}$) are significantly higher than bulk ceramic and MLCCs due to fewer defects and pores, as summarised in Table 6. Most research into lead-free ceramic thin films has focused on perovskite-type BT and BF-based compositions. High $W_{rec}$ $\sim 112$ J cm$^{-3}$ with $\eta$ $\sim 80\%$, along with good temperature stabilities between $-100$ to $150$ °C, was reported

**10772** | *Chem. Soc. Rev.*, 2024, **53**, 10761–10790

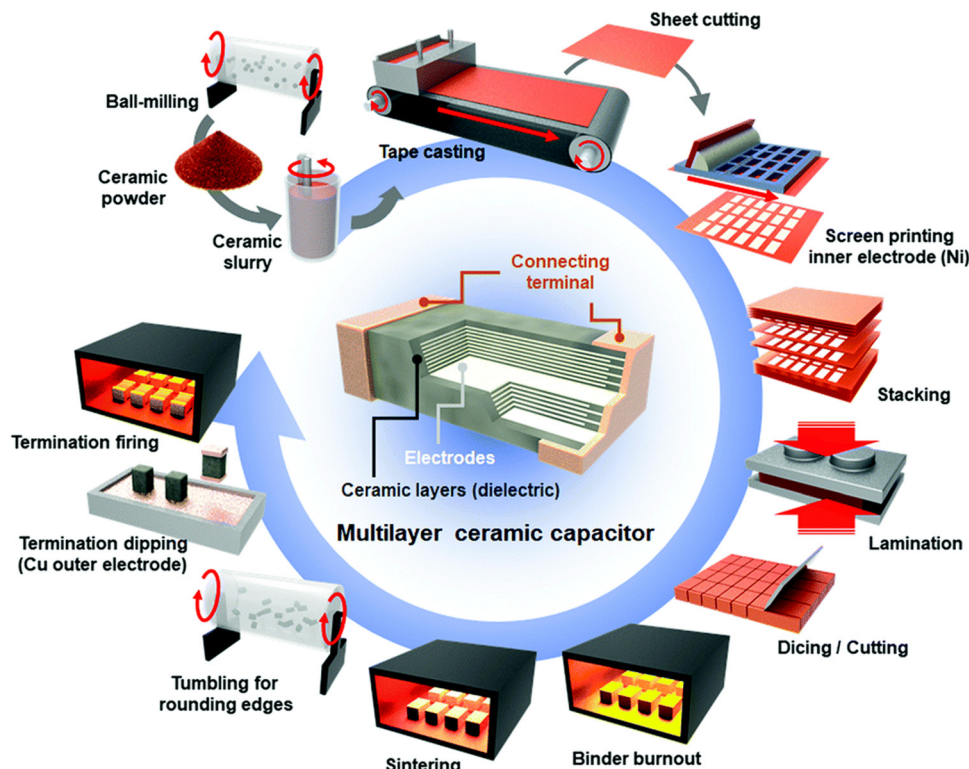This journal is © The Royal Society of Chemistry 2024

**Fig. 12** Schematics of the fabrication process with its construction.[194] Reproduced from ref. 194 with permission from the Royal Society of Chemistry.

**Table 5** Functional properties of the MLCCs from the literature

| Composition | $W_{rec}$ (J cm$^{-3}$) | $\eta$ (%) | $E$ (kV cm$^{-1}$) | $\Delta P$ ($\mu$C cm$^{-2}$) | $\tau_{0.9}$ (ns) | $P_D$ (MW cm$^{-3}$) | $\varepsilon_r$ at RT | $t$ ($\mu$m) | Electrode | Ref. |
|---|---|---|---|---|---|---|---|---|---|---|
| 0.88BT–0.12 Bi (Li$_{0.5}$Ta$_{0.5}$) O$_3$ | 4.1 | 95 | 466 | 25 | — | — | — | 30 | Pt | 198 |
| Ag (Nb$_{0.85}$Ta$_{0.15}$) O$_3$ + 0.25 wt.% MnO$_2$ | 7.9 | 71 | 1020 | 44 | — | — | — | 15 | Pt | 199 |
| 0.67NN–0.18NBT–0.15Bi (Mg$_{0.5}$Hf$_{0.5}$) O$_3$ | 12.7 | 88 | 1100 | 29 | 900 | 44 | 550 | 100 | 70 Ag/30Pd | 200 |
| 0.57BF–0.3BT–0.13 Bi (Li$_{0.5}$Nb$_{0.5}$) O$_3$ | 13.8 | 81 | 950 | 54 | — | — | | 10 | Pt | 201 |
| Sm$_{0.05}$Ag$_{0.85}$Nb$_{0.7}$Ta$_{0.3}$O$_3$ | 14.0 | 85 | 1450 | 20 | 900 | 103 | 440 | 10 | Pt | 71 |
| 0.87BT–0.13Bi [Zn$_{2/3}$(Nb$_{0.85}$Ta$_{0.15}$)$_{1/3}$] O$_3$ | 14.1 | 70 | 1500 | 35 | — | — | 900 | 5 | Pt | 202 |
| 0.5BF–0.4 ST–0.03Nb–0.1BMN | 15.8 | 75 | 1000 | 50 | — | — | 510 | 8 | Pt | 192 |
| 0.62NBT–0.3Sr$_{0.7}$Bi$_{0.2}$TiO$_3$–0.08BMN | 18.0 | 93 | 1013 | 54 | — | — | 1280 | 150 | Pt | 89 |
| 0.87BT–0.13Bi [Zn$_{2/3}$(Nb$_{0.85}$Ta$_{0.15}$)$_{1/3}$] O$_3$ + SiO$_2$ | 18.2 | 94 | 1755 | 35 | 450 | — | 920 | 10 | 60 Ag/40Pd | 203 |
| (Ba$_{0.33}$Bi$_{0.32}$Ca$_{0.11}$Sm$_{0.07}$Na$_{0.07}$Sr$_{0.1}$)(Ti$_{0.63}$Fe$_{0.32}$Zr$_{0.05}$)O$_3$ | 20.8 | 97 | 1094 | 49 | 11000 | — | 480 | 10 | 70Ag/30Pd | 204 |
| ⟨111⟩-textured 0.65NBT–0.35(Sr$_{0.7}$Bi$_{0.2}$) TiO$_3$ | 21.5 | 80 | 1030 | 65 | — | — | 2000 | 20 | Pt | 205 |
| 0.88NaNb$_{0.90}$Ta$_{0.10}$O$_3$–0.10ST–0.02La(Mg, Ti)O$_3$ | 43.5 | 85 | 2800 | 35 | — | — | 515 | 6 | Pt | 18 |

in a 450 nm-thick 0.25BF–0.3BT–0.45 ST thin film at $E_{max}$ ~4900 kV cm$^{-1}$, which the authors explained through the presence of a disordered crystal structure with mixed polymorphic nanodomains.[209] Non-perovskite-type dielectric thin films have also been reported with promising energy storage performance. A 350 nm-thick Aurivillius-type Bi$_{3.15}$Nd$_{0.85}$-Ti$_{2.8}$Zr$_{0.2}$O$_{12}$ thin film was optimised to deliver a high $\Delta P$ ~103 $\mu$C cm$^{-2}$ and $W_{rec}$ ~124 J cm$^{-3}$ with $\eta$ ~80% at $E_{max}$ ~3000 kV cm$^{-1}$ ref. 207 with fatigue-resistant up to 10$^9$ charge/discharge cycles and a wide temperature range of −100 to 200 °C. The best electrostatic energy storage performance to date, $W_{rec}$ ~182 J cm$^{-3}$ with $\eta$ ~78% at $E_{max}$ ~6200 kV cm$^{-1}$, was reported in 2022 by Lin *et al.* in a pyrochlore-type dielectric

thin film, Fig. 16(a and b).[210] The authors proposed this huge response was due to the growth of a high-entropy stabilised Bi$_2$Ti$_2$O$_7$-based dielectric film with the coexistence of multiple lattice distortions. The large $W_{rec}$ was attributed to the large $E_{max}$ (increased resistivity and breakdown properties) correlated with the presence of nano-crystalline grains and amorphous-like phases in the microstructure, as displayed in Fig. 16(c and d).

However, it is important to note that the mechanisms underlying the high polarisation values observed in thin films have not been fully evaluated. There is an urgent need for further investigation to understand why these thin films exhibit such large polarisation responses, as this could significantly
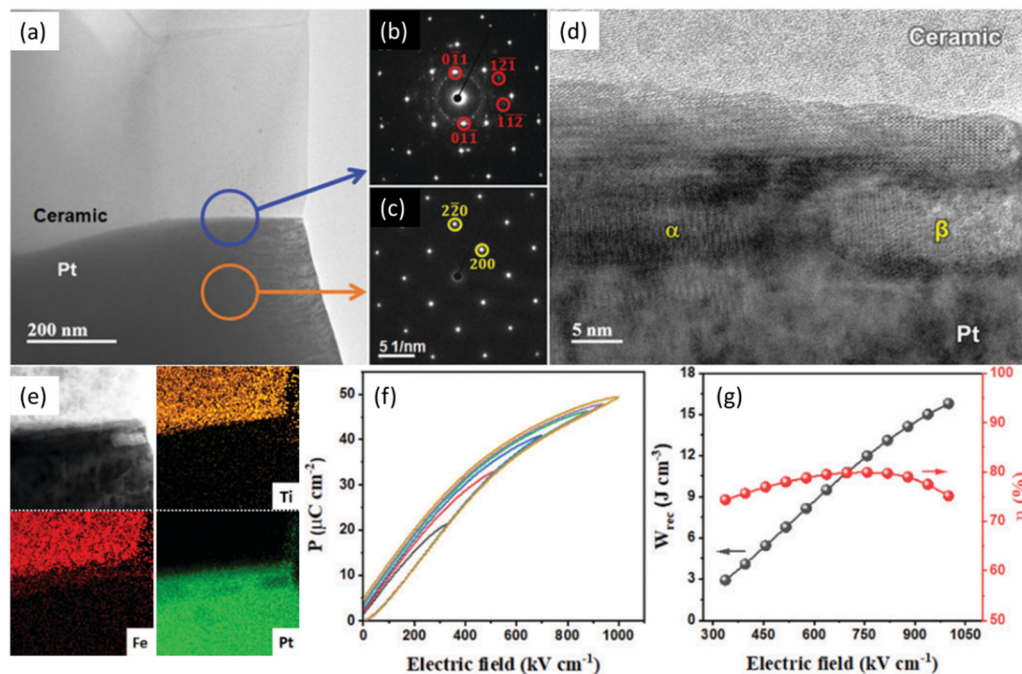
**Fig. 13** (a) TEM micrograph of BF−ST−Nb−0.1BMN/Pt interface. (b) SAD pattern highlighting BF−ST−Nb−0.1BMN reflections. (c) SAD pattern from Pt area in (a). (d) High-resolution TEM micrograph showing different phases at ceramic/Pt interface. (e) Bright-field STEM image and EDS elemental maps of ceramic/Pt interface. (f) Unipolar $P$−$E$ loops. (g) Energy storage properties ($W_{rec}$ and $\eta$) for BF−ST−Nb−0.1BMN multilayer.[192] Reprinted (adapted) with permission from ref. 192 under the terms of the Creative Commons Attribution 3.0 Unsupported Licence, Royal Society of Chemistry.



**Fig. 14** QLD type MLCCs performance. (a) Unipolar $P$−$E$ curves of NNTa$_{0.10}$−10ST−2LMT MLCCs up to the maximum field. (b) Polarisation maximum and increment as a function of electric field up to 280 MV m$^{-1}$. (c) Energy storage performance up to the maximum field. (d) The [001]-oriented atomic resolution HADDF-STEM images for NNTa$_{0.10}$−10ST−2LMT (QLD) with the projected polarisation angle. Individual arrows show B-site cation displacement vectors in individual unit cells with different vector angles.[18] Reprinted with permission from ref. 18, the John Wiley and Sons., under the terms of the Creative Commons CC BY license.

**Fig. 15** Energy storage of ANT + Mn multilayer capacitors. (a) Unipolar P–E loops and (b) $W_{rec}$ and $\eta$ measured at different electric fields from 200 kV cm$^{-1}$ to 1020 kV cm$^{-1}$.[81] Reproduced from ref. 81 with permission from the Royal Society of Chemistry.

**Table 6** Functional properties of thin film ceramics from the literature

| Composition | Substrate | $W_{rec}$ (J cm$^{-3}$) | $\eta$ (%) | $E$ (kV cm$^{-1}$) | $\Delta P$ (μC cm$^{-2}$) | $\varepsilon_r$ at RT | $t$ (nm) | Ref. |
|---|---|---|---|---|---|---|---|---|
| BaZr$_{0.35}$Ti$_{0.65}$O$_3$ | ITO layer | 40.6 | 69 | 4230 | 22 | 86 | 130 | 211 |
| Ag (Nb$_{0.45}$Ta$_{0.55}$)O$_3$ | Si (100) | 46.4 | 80 | 3300 | 34 | 130 | 300 | 212 |
| 0.4BF–0.6ST | Nb: STO | 51.0 | 60 | 3600 | 40 | 225 | 500 | 213 |
| Ba (Zr$_{0.35}$Ti$_{0.65}$)O$_3$ | LSMO + STO + F-Mica | 65.1 | 73 | 6150 | 28 | 141 | 130 | 214 |
| 0.88Ba$_{0.55}$Sr$_{0.45}$TiO$_3$ –0.12BMN | Nb: STO | 86.0 | 73 | 5000 | 51 | 240 | 400 | 216 |
| Ba$_{0.3}$Sr$_{0.7}$Zr$_{0.18}$Ti$_{0.82}$O$_3$ | Pt-coated Si | 89.4 | 65 | 6300 | 38 | 151 | 610 | 217 |
| Ba(Zr$_{0.35}$Ti$_{0.65}$)O$_3$ | Si | 93.5 | 71 | 8500 | 30 | 57 | 415 | 218 |
| Ba$_{0.95}$Sr$_{0.05}$Zr$_{0.2}$Ti$_{0.8}$O$_3$ | Pt/Ti/SiO2/Si | 102.0 | 87 | 6200 | 30 | 65 | 100 | 219 |
| 0.25BF–0.3BT–0.45 ST | (001)-oriented Nb: STO | 112.0 | 80 | 4900 | 57 | 250 | 450 | 209 |
| (Ba$_{0.95}$, Sr$_{0.05}$)(Zr$_{0.2}$, Ti$_{0.8}$)O$_3$ | Pt (111)/Ti/(100)Si | 148.0 | 91 | 6600 | 49 | — | 300 | 220 |
| (Bi$_{3.25}$La$_{0.75}$)(Ti$_{1.8}$Zr$_{0.4}$Hf$_{0.4}$Sn$_{0.4}$)O$_{12}$ | Pt (111)/Ti/SiO$_2$/Si | 182.0 | 78 | 6200 | 55 | 80 | 620 | 210 |

impact the future design and optimisation of high-performance dielectric materials.

## 3.4. Summary of state-of-the-art lead-free ceramics for high energy density capacitors

The development of lead-free dielectric ceramics for high-energy-density capacitors has seen significant progress over the past five years, as evidenced by the increasing number of publications (Fig. 2). The figure-of-merit ($W_{rec}$ and $\eta$) of these lead-free candidates is either equivalent to or outperforms their lead-based counterparts, although we note that much less research and optimisation have been performed on lead-based systems. Class-II capacitors for consumer electronics rely on BT but it offers lower $W_{rec}$ than competitor compositions.[14,15,221–225] Instead, there has been an explosion of lead-free candidates based on AFEs (NN and AN) and FEs (NBT and BF). Several promising bulk ceramic compositions based on NN and AN have successfully transitioned into MLCCs using powder-based synthesis methods (tape-casting). This success highlights the potential for larger-scale manufacturing of new lead-free high-energy-density capacitors. Comparatively, the $W_{rec}$ of ceramic thin films ($t < 1$ μm) surpasses that of bulk ceramics and MLCCs but this is attributed in the main to their higher breakdown strengths with $E_{max}$ an order of magnitude greater than in MLCCs.

**3.4.1. Comparison between lead-free bulk ceramics.** The energy storage performance metrics ($E_{max}$, $\Delta P$, $W_{rec}$ and $\eta$) of lead-free bulk ceramics are summarised and depicted in Fig. 17. $W_{rec}$ vs. $\eta$ (Fig. 17a) NN and NBT-based bulk ceramics currently demonstrate superior performance, exhibiting $W_{rec} > 8$ J cm$^{-3}$ and $\eta > 80\%$. AN-based bulk ceramics present lower $W_{rec}$ ($< 8$ J cm$^{-3}$) and lower $\eta$ ($< 80\%$). The $W_{rec}$ for BF-based bulk ceramics displays variable values, with a few instances below 5 J cm$^{-3}$ with $\eta < 60\%$, attributed to the opening of the P–E loop (potentially indicating a high leakage). In Fig. 17b, a comparison of $W_{rec}$ vs. $E_{max}$ reveals that NN-based bulk ceramics currently offer the highest $E_{max}$ (up to 980 kV cm$^{-1}$), partially due to their large intrinsic bandgap, followed by NBT, AN, and BF which along with a homogeneous electrical microstructure yields a high $E_{max}$. Lead-free dielectric ceramics for high energy density capacitors can be categorised based on the required voltage, with NN being the preferred choice for high voltage (equivalent to electric field $> 800$ kV cm$^{-1}$) capacitors, while NBT is the optimal candidate for intermediate voltage (equivalent to electric field between 400 to 800 kV cm$^{-1}$) capacitors. Additionally, we note that $E_{max}$ is closely associated with thickness, which may affect the comparison between each lead-free candidate. Fig. 17c illustrates the comparison between $W_{rec}$ and $\Delta P$ for lead-free bulk ceramics. NBT-based bulk ceramics exhibit the highest $\Delta P$ (up to 62 μC cm$^{-2}$), followed by AN, BF and NN. The high $W_{rec}$ of NBT-based materials is influenced by their substantial $\Delta P$ which is influenced by the electrode area. It is therefore important to consider such information for an accurate comparison. Fig. 17d illustrates

This journal is © The Royal Society of Chemistry 2024

Chem. Soc. Rev., 2024, 53, 10761–10790 | 10775
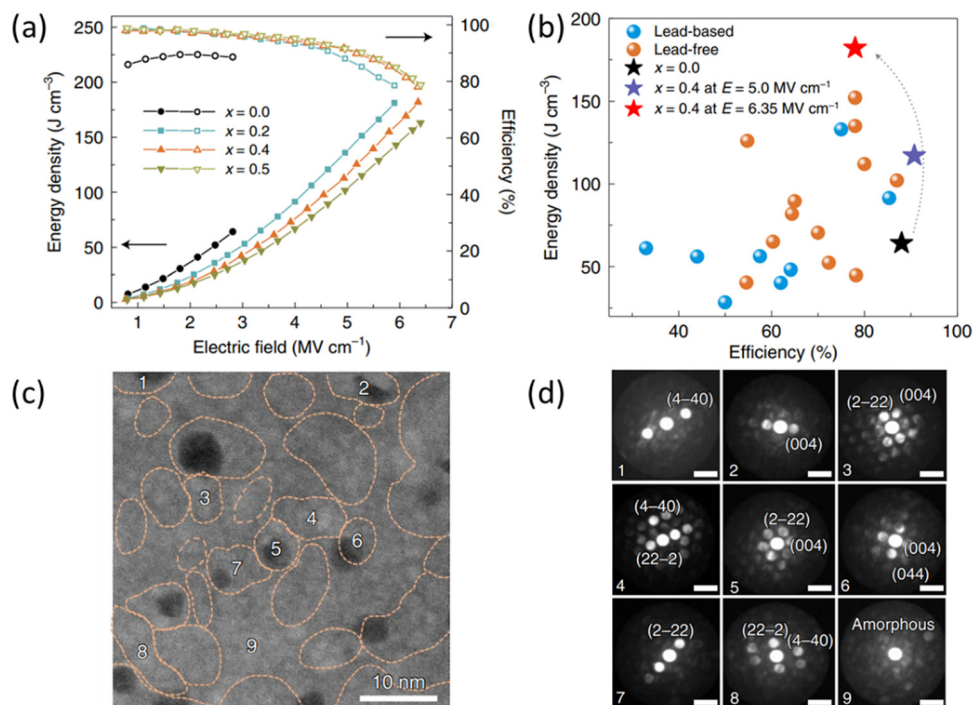
**Fig. 16** (a) Energy density and efficiency as functions of electric field up to breakdown strength. (b) Comparison of the energy density and efficiency of our films with representative dielectrics. (c) Low-magnification HAADF image of the ceramic thin film, showing the coexistence of nano-crystalline grains (numbered 1–8) and an amorphous-like phase (no. 9). (d) Nano-beam electron diffraction patterns of the nano-crystalline grains and amorphous-like phase labelled by 1–9 in (c).[210] Reproduced from ref. 210 with permission from Springer Nature.
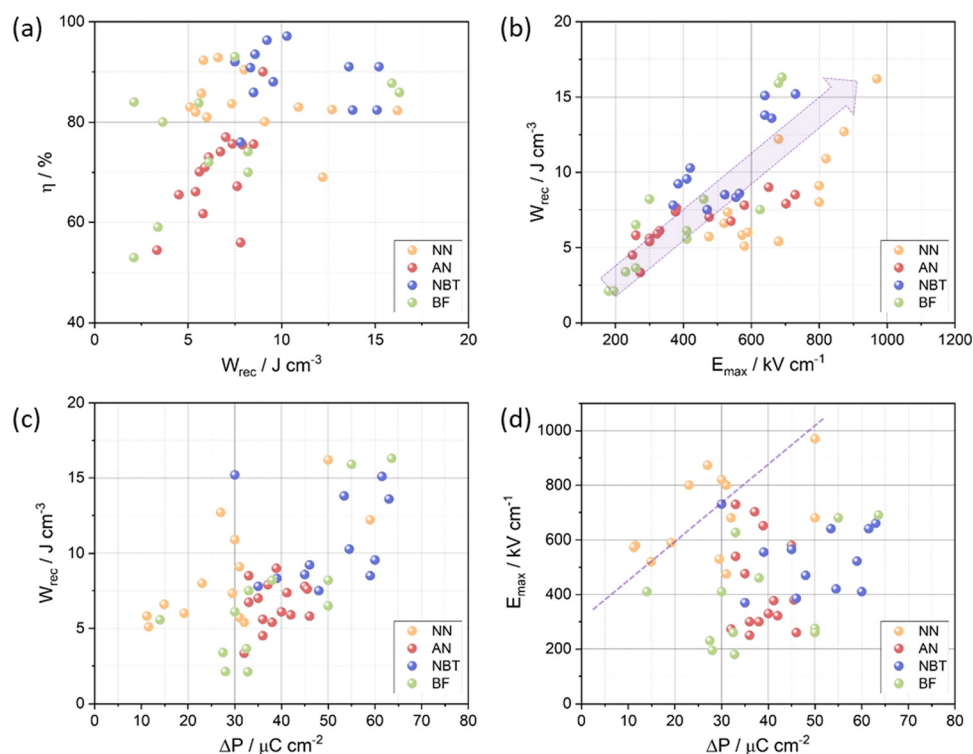


**Fig. 17** Comparison between (a) $W_{rec}$ vs. $\eta$ (b) $W_{rec}$ vs. $E_{max}$ (c) $W_{rec}$ and $\Delta P$ (d) $E_{max}$ vs. $\Delta P$ in different bulk ceramics.

10776 | Chem. Soc. Rev., 2024, 53, 10761–10790

This journal is © The Royal Society of Chemistry 2024

**Fig. 18** The comparison between (a) $E_{max}$ and $W_{rec}$ and (b) $W_{rec}$ and $\eta$ in terms of thickness.

$E_{max}$ *vs.* $\Delta P$ for a wide range of compositions. NN-based bulk ceramics cluster above the diagonal line due to their high $E_{max}$ and low $\Delta P$, whereas NBT, BF, and AN-based bulk ceramics are primarily situated below the diagonal line signifying high $\Delta P$ and low $E_{max}$.

**3.4.2. Comparison between bulk ceramics, MLCCs and ceramic thin films.** The current state-of-the-art values for $W_{rec}$ in bulk ceramics, multilayer ceramic capacitors (MLCCs), and ceramic thin films are reported as 16 J cm$^{-3}$, 43.5 J cm$^{-3}$, and 182 J cm$^{-3}$, respectively. As of 2024, the $W_{rec}$ for bulk ceramics and MLCCs has witnessed a remarkable improvement but the $W_{rec}$ for ceramic thin films surpasses that of both bulk ceramics and MLCCs by >5x. This significant difference is primarily

attributed to the larger $E_{max}$ (Fig. 18a) which is enhanced by the reduced thickness (different fabrication techniques). The thickness of bulk ceramics, MLCCs, and ceramic thin films is approximately 50–150 μm, 5–20 μm, and 0.1–0.6 μm, respectively. Consequently, it becomes imperative to normalise $W_{rec}$ with respect to thickness for a more appropriate comparison across different lead-free ceramics (including bulk ceramics, MLCCs, and thin films).

**3.4.3. The effect of thickness on energy storage performance.** The impact of thickness on $E_{max}$ and $W_{rec}$ among lead-free bulk ceramics is presented in Fig. 19a. As the thickness of bulk ceramics decreases from 200 to 50 μm, $E_{max}$ increases fourfold, ranging from approximately 250 to



**Fig. 19** Impact of thickness on (a) $E_{max}$ (b) normalised $W_a = W_{rec}/E_{max}$ and $\eta$ in NN, AN, NBT, and BF-based ceramics (c) normalised $W_a$ with $\eta$ (d) normalised $W_a$ with $\Delta P$ in bulk ceramics, MLCCs, and thin films.

This journal is © The Royal Society of Chemistry 2024

*Chem. Soc. Rev.*, 2024, **53**, 10761–10790 | **10777**

**Review Article**

View Article Online

**Chem Soc Rev**

$1000$ kV cm$^{-1}$. To mitigate the thickness effect, $W_{rec}$ is normalised by $E_{max}$ ($W_a = W_{rec}/E_{max}$), as depicted in Fig. 19b. NBT-based bulk ceramics, situated in the top right corner (high $W_a$ and $\eta$), currently exhibit the best-normalised $W_a$ (up to 0.025) and $\eta$ ($> 80\%$) due to the higher $\Delta P$ under the same electric field for NBT-based bulk ceramics. The comparison of normalised $W_a$ with $\eta$ and $\Delta P$ is illustrated in Fig. 19c and d. The normalised $W_a$ values are concentrated in a range from 0.01 to 0.025. From Fig. 4, the $W_{rec}$ (area to the left of unipolar $P$–$E$ loop) is equal to half of the product between $E_{max}$ and $\Delta P$. $W_a$ thus exhibits a linear relationship to the $\Delta P$ ($W_a = 0.5 \times \Delta P$), as displayed in the black solid line in Fig. 19d. The majority of the reported AFE and RFE dielectrics, regardless of the thickness, follow this line with slope $k < 0.5$., mainly due to the energy loss and curve of the $P$–$E$ loop during electrical charging and discharging.

**3.4.4. The effect of electrode area on energy storage performance.** Zhang and co-authors[20] proposed in 2023 that the size of the electrode area has a significant impact on $\Delta P$ as well as $W_{rec}$. The influence of electrode area on $\Delta P$ and $W_{rec}$ is examined among bulk ceramics, MLCCs and ceramic thin films. The relationship between electrode area and $\Delta P$ is displayed in Fig. 20a. As the electrode area decreases from 0.12 to 0.075 cm$^2$, $\Delta P$ doubles from 20 to 40 μC cm$^{-2}$ on average. The $W_{rec}$ is again normalised by $\Delta P$, $W_b = W_{rec}/\Delta P$, to account for the electrode area effect. Fig. 20b shows that NN-based bulk ceramics, situated in the top right corner

(high $W_b$ and $\eta$), currently offer the best-normalised $W_b$ (up to 0.47) and $\eta$ ($> 80\%$). The comparison of normalised $W_b$ with $\eta$ and $\Delta P$ is illustrated in Fig. 20c and d. $W_b$ is 0.1 to 0.5 (Fig. 20c) across all bulk ceramics, MLCCs as well as some ceramic thin films. $W_b$ is also found to demonstrate a linear relationship with $E_{max}$ ($W_b = 0.5 \times E_{max}$), as shown by the black solid line in Fig. 20d. The majority of the non-linear AFE and RFE dielectrics demonstrate a linear relationship between $W_b$ and $E_{max}$ with slope $k < 0.5$.

The electrode area information is commonly provided in recent studies on bulk ceramics, as it influences polarisation during electrical $P$–$E$ measurements. However, this crucial parameter is often ignored or unreported in ceramic thin film and MLCC studies. The determination of the effective dielectric layer thickness in MLCCs and ceramic thin films commonly relies on direct measurements from SEM images. However, discrepancies may arise when estimating electrode areas, often leading to calculation errors in energy storage assessments. From this perspective, we propose that evaluating electrode area is equally important as ceramic thickness and is critical for electrical measurements to accurately assess energy storage.

# 4. Strategies for optimising energy storage performance

Achieving an optimal balance among various parameters is essential for improving energy storage. The enhancement of
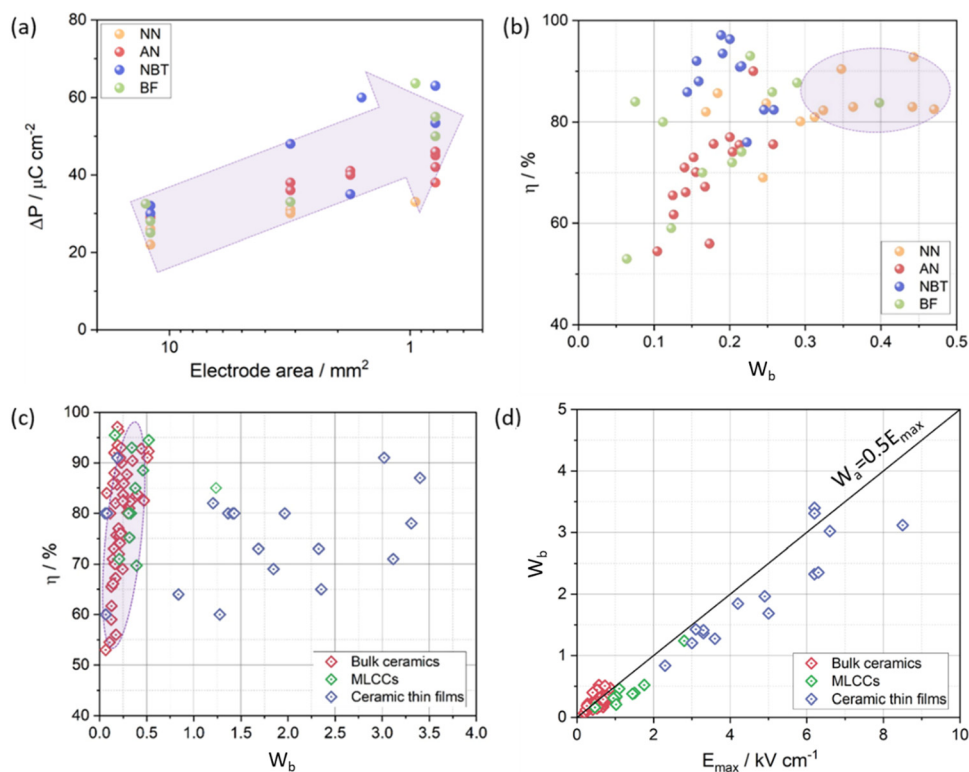


**Fig. 20** The relationship between (a) electrode area and $\Delta P$ in NN, AN, NBT, and BF-based ceramics (b) normalised $W_b$ and $\eta$ in NN, AN, NBT, and BF-based ceramics (c) normalised $W_b$ and $\eta$ in bulk ceramics, MLCCs, and thin films (d) normalised $W_b$ and $E_{max}$ in bulk ceramics, MLCCs, and thin films.

**10778** | *Chem. Soc. Rev.*, 2024, **53**, 10761–10790

This journal is © The Royal Society of Chemistry 2024

energy density typically compromises efficiency, and *vice-versa*. Recent studies underscore that securing a high $E_{max}$ is critical, even at the expense of a reduced $\Delta P$. As highlighted in the preceding summary, diminishing sample thickness can mitigate defects, thereby substantially enhancing $E_{max}$. To obtain ceramics with high density and fine grain size, numerous methodologies have been documented, including Repeated Rolling Processing (RRP),[159,165,168] two-step sintering,[184] and the incorporation of Bi-based constituents as sintering aids.[55,64] Besides optimisation of density and microstructure, the following strategies are also crucial for improving energy storage.

### 4.1. Optimisation of electrical properties

The substitution of NN in BF–BT bulk FEs has been shown to increase the band gap.[30] Moreover, NN-based materials not only exhibit inherently superior $E_{max}$ compared to other systems, as highlighted in the preceding summary, but their wide band gap has also shifted research focus towards reducing resistivity.[29]

Incorporating manganese (Mn) into AN-, NN-, and BF-based material systems is a strategy widely adopted to enhance resistivity,[68,69,117,187,226–228] and is especially crucial for BF-based materials due to their susceptibility to high leakage currents.[229,230] Inspired by techniques employed in lead-based materials, manganese oxides function as electron traps to improve resistivity (as shown in Fig. 21(a) where Mn is doped in NN–SrSnO$_3$)[49] and as a grain-size refiner.[231–233] Tantalum (Ta) has been reported as a promising dopant to enhance resistivity and activation energy in AN- and NN-based materials.[38,84,153,198] Additionally, due to the refractory nature of Ta$_2$O$_5$, Ta can also reduce grain size, which is beneficial for achieving higher breakdown strength ($E_{max}$) (Fig. 21(b)).[75]

Research on interfacial polarisation (Maxwell–Wagner polarisation caused by space charge in heterogeneous systems) restriction in NBT–BT ceramics,[158] has shown that decreasing the resistivity difference between grains and grain boundaries achieves electrical homogeneity like those in BF-based systems.[181,234] Impedance spectroscopy, a valuable method for evaluating the electrical homogeneity of materials, has been utilised in various energy storage dielectric materials, including BF-, NBT-, and NN-based ceramics.[31,51,59,60,63,158,166,178,235] Impedance spectroscopy can demonstrate when the imaginary parts of impedance ($Z''$) and electrical modulus ($M''$) overlap, a signal for electrical homogeneity across ceramics. In conclusion, the synergistic enhancement of $E_g$, $E_a$, and the presence of a homogeneous electrical microstructure, play a pivotal role in boosting $E_{max}$.

### 4.2. Disruption of long-range polar order

Optimising factors such as high density, small grain size, and electrical properties are crucial, but another critical aspect is the disruption of the long-range polar order in the material matrices sometimes referred to as phase or domain engineering. This strategy attains a high $\eta$ but reduces $P_{max}$ due to the onset of relaxor behaviour in which PNRs, rather than macro-domains minimise polarisation switching hysteresis, leading to slimmer $P$–$E$ loops.

Fig. 22 illustrates the common strategies used across various dielectric systems to disrupt long-range polar order, showing general trends rather than specific examples for each material. The disruption of long-range polar order, phase transitions, and domain structure discussed here are widely applicable across AN, NN, BF, and NBT systems, making such a generalised approach appropriate.

For AN- and NN-based AFE materials, doping or the introduction of solid solutions can lower the temperature onset of phase transitions such as M2, and M3 for AN-based and R and Q phase for NN-based.[28,42,78,80,183,236,237] Simultaneously, dopants disrupt long-range antipolar order, resulting in smaller domains, leading to reduced $P_r$ minimising electro strain and driving higher efficiency through slimmer loops associated with the field-induced FE phase. Using this approach, an ultrahigh $E_{max}$ of $\sim 1450$ kV cm$^{-1}$ and an outstanding $W_{rec}$ of about 14 J cm$^{-3}$ with an $\eta$ of approximately 85% were realised in Sm$_{0.05}$Ag$_{0.85}$Nb$_{0.7}$Ta$_{0.3}$O$_3$ MLCCs.[71]

In BF- and BNT-based perovskites, the tilting of oxygen octahedra often impedes domain reorientation, as evidenced



**Fig. 21** (a) Nyquist-plot of the NN, NN−5SrSnO$_3$, NN−5SrSnO$_3$_0.1Mn, and NN−5 SrSnO$_3$_1.0Mn samples.[49] (b) The composition dependence of average grain size and $E_b$, the insets give the SEM micrographs of the AN and AN−Ta$_{0.55}$ ceramics, respectively.[77] Reprinted with permission ref. 49 from under the terms of the Creative Commons CC BY license, Springer Nature. Reprinted with permission from ref. 77, under the terms of the Creative Commons CC BY license, Springer Nature.

This journal is © The Royal Society of Chemistry 2024

*Chem. Soc. Rev.*, 2024, **53**, 10761–10790 | **10779**

**Fig. 22** Schematic microstructure and unipolar $P$–$E$ loops (with the same internal electric between red, green, and blue) of different dielectrics for electrostatic energy storage (evaluated by the area of red, green and blue) (a) FE with macroscopic domains ($dP/dE = 0$) (b) RFE with multiple polar nanoregions ($dP/dE \rightarrow 0$). (c) QLD behaviour with lattice distortions ($dP/dE$ = constant, $k$).[18] Reprinted with permission from ref. 18, the John Wiley and Sons., under the terms of the Creative Commons CC BY license.

by the large coercive field ($E_C$). By combining a FE component with significant structural distortion ($\delta$) and a paraelectric (PE) component to create an RFE with a t close to 1, it is possible to achieve exceptionally high $W_{rec}$ and high $\eta$ simultaneously.[161] Additionally, doping with ions of varying valence, electronegativity, and ionic radii may induce significant local lattice disorder, leading to the disruption of long-range polar order and the formation of PNRs, thereby substantially reducing $P_r$.[182]

### 4.3.  High entropy enhancement

Since 2004, the concept of disordered multicomponent systems emerged, aiming to maximise configurational entropy and stabilise equimolar mixtures, leading to the development of high-entropy materials. Initially explored in metal alloys and nitride films, entropy stabilisation was later demonstrated in oxides in 2015, spurring the rapid development of high-entropy disordered ceramics. Highly disordered, multi-component systems benefit from high entropy, leading to preferred single-phase solid solutions, sluggish kinetics, lattice distortions, and superior properties. This versatility enables the enhancement of properties by tailoring the compositions of the ceramics in the field of high-energy dielectric ceramic capacitors.

Derived from the Gibbs free energy, the relationship between the atomic fraction of elements and entropy of mixing is shown below, where $\Delta S_{mix}$ is the entropy of mixing, $R$ is the gas constant, and $N$ is the total number of elements, yielding the results for single phase materials usually.[238]

$$\Delta S_{mix} = R \ln N \qquad (8)$$

$S_{mix}$ reaches a maximum when all elements are present in an equiatomic 5-cation system, the maximum $S_{mix}$ value that can

be achieved is 1.61 $R$. As per empirical classification, based on its configurational entropy introduced by Murty *et al.*,[239] https://onlinelibrary.wiley.com/doi/full/10.1002/adma.201806236-adma201806236-bib-0012 materials with $S_{mix} \geq 1.5$ $R$ can be classified as "high entropy", materials with $1.5\ R > S_{mix} \geq 1\ R$ as "medium entropy" and materials with $S_{mix} < 1\ R$ as "low entropy" systems. When $S_{mix} \geq 1.5\ R$, a single phase is often attained, as the magnitude of $T\Delta S_{mix}$ becomes significant enough to surpass enthalpy, $\Delta H_{mix}$, which is dependent on the free energy of the system ($\Delta G_{mix}$) particularly at elevated temperatures ($T$), as shown in eqn (9). This underscores the importance of high temperatures in facilitating the formation of high or medium entropy (single-phase) systems; however, many of these systems are deemed metastable at room temperature.[238]

$$\Delta G_{mix} = \Delta H_{mix} + T\Delta S_{mix} \qquad (9)$$

In bulk materials, notable successes using a 'high-entropy' approach are exemplified in KNN- and NBT-based ceramics, and recently a BT-based MLCC[204] which exhibits relaxor behaviour. In KNN-based ceramics, combining the high-entropy strategy with meticulous preparation optimisation yields rhombohedral–orthorhombic–tetragonal–cubic multiphase nanoclusters, as depicted in Fig. 23. These nanoclusters host ultra-small polar nanoregions (PNRs), resulting in an unprecedented $W_{rec} \sim 10.06$ J cm$^{-3}$ and an ultra-high $\eta$ of approximately 90.8%.[240] Conversely, in NBT-based ceramics, the high-entropy approach vacates multiple oxygen octahedron tilts, enhancing the random field and significantly delaying polarisation saturation. This facilitates easier polarisation reorientation under external electric fields, reducing heat generation and enhancing thermal breakdown strength,

Fig. 23 Schematic overview of high-entropy design approach for KNN-based ceramics.[240] Reprinted (adapted) with permission from ref. 240 under the terms of the Creative Commons CC BY license, Springer Nature.

leading to an exceptional $W_{rec} \sim 13.8$ J cm$^{-3}$ and a high efficiency ($\eta \sim 82.4\%$).[171] Extending beyond bulk ceramics, the high-entropy strategy has been applied to thin films based on bismuth titanate ($Bi_2Ti_2O_7$, Fig. 16) and MLCC-based on $(Ba_{0.33}Bi_{0.32}Ca_{0.11}Sm_{0.07}Na_{0.07}Sr_{0.1})(Ti_{0.63}Fe_{0.32}Zr_{0.05})O_3$ with entropy $> 2.38R$ providing high $W_{rec}$ value of 20.8 J cm$^{-3}$ with an ultrahigh $\eta$ of 97.5%.

High entropy compositions have multiple components occupying the A or B-site which is the same effective approach used in the formation of many relaxors. The characteristics of multiple polar clusters at the local scale reported in 'high-entropy' bulk ceramics, MLCCs and ceramic thin film are comparable to PNRs in relaxor which can be induced through multiple occupancy of A and B- sites of the perovskite structure. Therefore, the comprehensive implementation of the high-entropy strategy across different material systems does require further clarification and investigation. Although it has been claimed to be an optimisation strategy for energy density performance, it appears to be qualitatively similar to approaches in the literature reported over the last decade which are often described as pseudo-ternary, quaternary and quinary (or more) perovskite solid solutions,[241–244] rather than as a single formula unit.

### 4.4. Processing innovation

High electro-strain in AFEs and REFs is considered a potential threat for practical applications for high field/energy density

capacitors during AC/DC cycling and may cause mechanical failure along the interface between internal electrodes and ceramic layers, leading to poor MLCC reliability and early breakdown. Li and co-authors[205] fabricated grain-orientated NBT-SBT MLCCs using an ST template, Fig. 24(a and b). The textured MLCCs exhibited reduced electro strain ($< 0.2\%$) in comparison to $> 0.5\%$ in untextured samples, Fig. 24(c and d), realising enhanced $W_{rec} \sim 21.5$ J cm$^{-3}$ at $E_{max} \sim 1030$ kV cm$^{-1}$.

Low $\eta$ not only leads to a high $W_{loss}$ but may also generate self-heating during charge–discharge, leading to electrical breakdown.[245] A 'sandwich' MLCC structure, designed to optimise $\eta$ composed of mixed layers of 0.35BF–0.65 ST and BNST has been reported by Yan and co-authors,[246] realising improved $W_{rec} \sim 9.05$ J cm$^{-3}$ with high $\eta = 97\%$ at 710 kV cm$^{-1}$, Fig. 25.

## 5. Current challenges and future perspectives

### 5.1. Materials challenge for temperature stability

The thermal stability of dielectric materials exhibiting high energy/power density is a crucial factor for practical applications in portable electronics, electric vehicles, and pulsed power systems. Polymer-based dielectric materials offer high power/energy density at ambient temperatures, but above 100 °C, they become unreliable and susceptible to dielectric breakdown. Consequently, ceramic-based dielectric materials are prioritised and receiving increased attention due to their
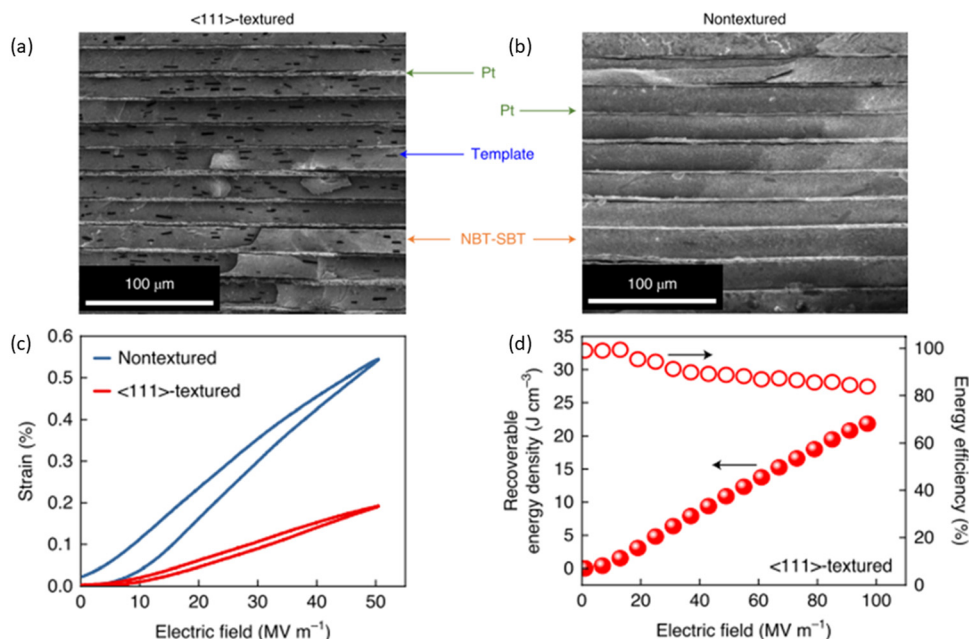
This journal is © The Royal Society of Chemistry 2024

*Chem. Soc. Rev.*, 2024, 53, 10761–10790 | 10781

**Fig. 24** SEM cross-section of (a) textured and (b) untextured NBT-SBT MLCCs. (c) $S–E$ Loops of textured and nontextured MLCCs. (d) The energy storage performance of textured NBT-SBT MLCCs.[205] Reproduced from ref. 205 with permission from Springer Nature.
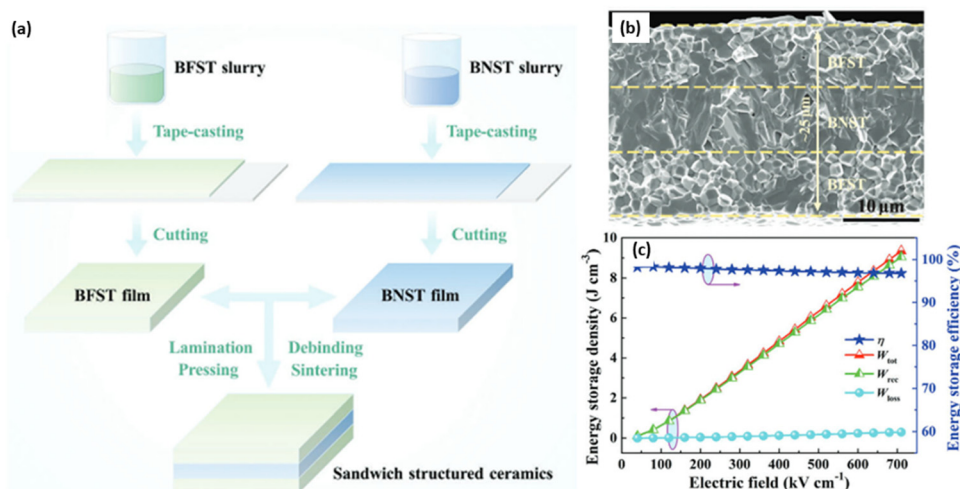


**Fig. 25** (a) Schematic illustration for preparing the sandwich BFST/BNST/BFST ceramics by tape-casting method; (b) SEM cross-section image of sandwiched structured ceramics; (c) energy storage performance of sandwiched structured ceramics.[246] Reproduced from ref. 246 with permission from the John Wiley and Sons.

high polarisation, rapid charge–discharge speed ($<$ns), and superior thermal stability.

The temperature stability of high energy density ceramics is often evaluated by performing temperature-dependent $P–E$ measurements, simulating the environmental conditions in high-voltage capacitors. The applied electric field during temperature studies is approximately 1/4 to 1/2 of the maximum field ($E_{max}$), and the stability benchmark refers to a variation in $W_{rec}$ of less than 15%. Temperature stability performance for bulk ceramics has been summarised and plotted in Fig. 26.

Currently, the maximum operating temperature is 200 °C in a few NN and NBT-based bulk ceramics which offer the best average temperature stability of 160 ± 40 °C, compared to $\sim$110 ± 30 °C found in BF and AN-based ceramics. Recently, broad temperature stability ($<$10%) has also been reported in a NN based MLCCs, $0.88Na(Nb_{0.90}Ta_{0.10})O_3$–$0.1ST–0.02La(Mg,Ti)O_3$, up to 200 °C with $W_{rec} \sim 15$ J cm$^{-3}$.[18]

Two significant challenges have been identified for high-temperature operation: (i) premature mechanical/dielectric breakdown and (ii) low charge–discharge energy efficiency

**10782** | *Chem. Soc. Rev.*, 2024, **53**, 10761–10790

This journal is © The Royal Society of Chemistry 2024

**Fig. 26** Correlation between max temperature stability and $W_{rec}$ among four lead-free dielectric candidates.

($\eta < 60\%$). $W_{rec}$ often decreases at elevated temperatures, as evidenced by the opening of the $P$–$E$ loops (reduced $\eta$) or electrical breakdown (reduced $E_{max}$). Premature dielectric/mechanical breakdown can be attributed to the electric field-induced phase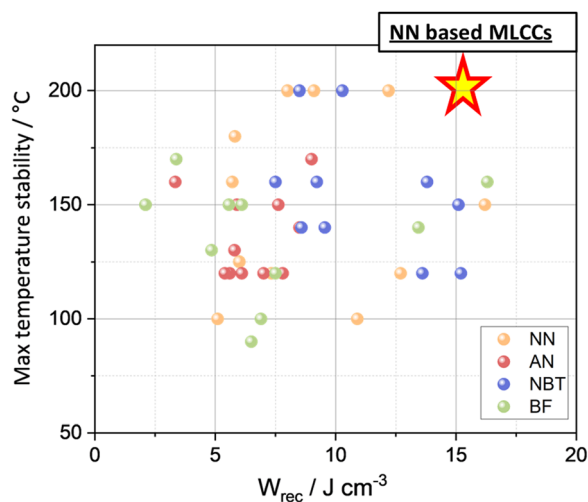 switching between AFE/RFE to FE phases. Substantial electrostrain is often developed during domain reorientation and/or structural transformation from PNRs to long-range orders during high field/voltage charge–discharge electrical cycling, leading to microcrack formation along the interface between electrodes and ceramics. The decrease in $\eta$ may be associated with changes in the correlation length (*e.g.* from short-range to meso-range) or to the motion of oxygen vacancies $V_o$ (Under combined high voltage and temperature conditions, both electrical and thermal breakdown mechanisms may occur simultaneously when dielectric ceramics can no longer maintain electrical insulation. However, there is a lack of in-depth studies, such as *in situ* poling diffraction/scattering with pair distribution function (PDF) analysis and high-resolution scanning transmission electron microscopy (STEM), to reveal such features under combined thermal (up to 200 °C) and electrical loading at high electric field levels (up to 400 kV cm$^{-1}$).

### 5.2. Process challenge on the co-fire compatibilities between dielectric ceramics with cost-effective inner electrodes

Precious metal electrodes (PMEs) like Pt or Ag/Pd (high level of Pd) are currently used as internal electrodes in most of the MLCCs reported in the literature (Table 5 above) whereas, base metal electrodes (BMEs) such as Ni or Cu, are employed in 99% of Class II high-permittivity commercial capacitors. An issue of incompatibility of BMEs with all current high energy density/voltage capacitors poses a serious challenge to achieving scalable manufacturing and system integration. Although PMEs offer robustness and long-term reliability, BMEs present a cost-effective solution for mass production.

Most lead-free dielectric ceramics can be sintered with a selection of PMEs in the air without any reaction. However, Pt is too expensive for industrial manufacturing and the recent spike in Pd price, from approximately $14.3 per gram in 2012 to $30.7 per gram in 2024,[245] also brings significant cost concerns for MLCC manufacturing. In contrast, the overall price trend for BMEs (Ni) between 2012 and 2021 has remained stable, approximately $0.02 per gram,[247] making them a more sensible option for MLCC mass production. The high melting point of Ni ($\sim$1455 °C) allows co-firing capability with dielectric ceramics requiring high sintering temperatures (*i.e.* >1200 °C for BT).[248] To date, none of the reported high-energy density MLCCs have used Ni as internal electrodes. The reaction between the Ni electrode and Bi-contained dielectric materials, *e.g.*, BF and NBT, at high temperatures results in the formation of low-resistivity and high-loss impurities. Although controlling both temperature and atmosphere (pO$_2$) is highly complicated and dependent on the specific dielectric ceramic material, exploring co-fire compatibilities with BMEs is still the prioritised research focus to overcome this challenge, particularly for those Bi-free MLCCs cases (NN/AN-based). Co-firing of KNN-based piezoelectric multilayers with Cu internal electrodes has however been reported by Randall and co-authors.[249]

In addition to exploring the processing conditions with BMEs, a secondary research focus is to reduce the sintering temperature to <950 °C, allowing co-firing with Ag/10%Pd internal electrodes. Incorporating sintering aids such as glass, dopants, and/or alloying with other members encourages ceramic densification at lower temperatures by forming liquid phases.[250] For example, adding a third component of Bi(Li$_{0.5}$Nb$_{0.5}$)O$_3$ into BF–BT effectively reduces the sintering temperature to 890 °C, allowing the possibility to co-fire with Ag or Ag/10%Pd. CuO was also reported to lower the sintering temperature of KNN-based piezoelectric ceramics to approximately 940 °C.[251]

## 6. Summary and perspectives

### 6.1. $E_{max}$ and equivalent voltage

$E_{max}$ has been frequently reported for various dielectric ceramics, including bulk, MLCCs and thin films while an assessment of the equivalent voltage has not received adequate attention. Bulk ceramics offer the highest voltage range for capacitors, averaging between 3 to 5 kV, followed by MLCCs (1.0 to 1.6 kV). Ceramic thin films, on the other hand, provide the lowest voltage range (0.05 to 0.20 V) due to their reduced thickness. Presently, commercial high-voltage capacitors offer a range of 400 to 800 V. State-of-the-art MLCCs now meet future voltage requirements for many high voltage/energy density applications but are limited by either the use of PME internal electrodes or their temperature stability is insufficient. In contrast, the PVD routes required to fabricate ceramic thin films are expensive and may only experience exploitation when directly integrated into Si technology.

This journal is © The Royal Society of Chemistry 2024

*Chem. Soc. Rev.*, 2024, **53**, 10761–10790 | **10783**

## 6.2. Temperature stability

NN and NBT-based bulk ceramics currently offer the best average temperature stabilities of $160 \pm 40$ °C, while AN and BF-based bulk ceramics experience $>15\%$ drops in $W_{rec}$ at temperatures above 150 °C. The electric field applied in almost every temperature study reaches only 1/4 to 1/2 of the $E_{max}$, equivalent to 1–2 kV for bulk ceramics and 0.4–0.8 kV in MLCCs, which is too low for practical applications. To enhance temperature stability, further research is required to understand field-induced AFE/FE and short- to long-range phase transitions. Most importantly, the defect chemistry which controls the conductivity at higher fields and temperatures requires further investigation.

Currently, there is a lack of *in situ* structural and electrical microstructural analysis under high field and temperature which modifies the operating conditions of a capacitor. More advanced structural analysis techniques, *e.g.*, synchrotron X-ray/neutron scattering, high-resolution STEM, *in situ* Raman spectroscopy, and local probe atomic force microscopy, as well as advanced electrical microstructural analysis techniques *e.g.*, local probe impedance, are desirable for further understanding temperature instabilities and dielectric/mechanical breakdown mechanism(s) under high fields and high temperatures. Additionally, there is a critical need to investigate the intrinsic polarisation mechanisms in lead-free dielectric/ferroelectric ceramics to better understand the origins of ultrahigh polarisation values reported in some materials.

## 6.3. Charge–discharge efficiency ($\eta$)

Low $\eta$ implies high energy consumption during electrical charging and discharging, which is not ideal for AC/DC cycles. NBT currently offers the highest $\eta$ of $\sim 89\%$, followed by NN ($\sim 84\%$), BF ($\sim 75\%$), and AN ($\sim 71\%$). Recent studies have focused more on RFE-type dielectrics, *e.g.*, NBT, realising high $\eta$ over AFE-type dielectrics (*e.g.*, AN and NN). To understand the origin of low $\eta$ at room or elevated temperatures, the local structural analysis and electrical microstructure of dielectric ceramics must be closely examined. Possible reasons include electric field-induced phase transition(s), motion of oxygen vacancies, changes in resistivity, capacitance, activated energy and electrical homogeneity.

## 6.4. MLCC development

The chemical reaction between Bi-based dielectrics and low-cost internal electrodes, such as Ag and Ni (under a controlled atmosphere), significantly restricts their potential for large-scale manufacture. AN and NN-based dielectrics offer the possibility of co-firing with cost-effective (BME) electrodes, although Ag/30Pd and Pt were still used in the literature. For AN and NN-based ceramics, glass additions could be used to reduce the sintering temperature, increasing compatibility with cost-effective electrodes. This would also decrease resistivity in grain boundaries, increase density and create a more uniform microstructure, all of which enhance the breakdown strength of the ceramic layers.[249] Similar strategies have been successfully employed in BT MLCCs. Recent developments in

academia and industry have focused on improving the volumetric efficiency and reliability of MLCCs, driven by the demand for advanced electronics and electric vehicles. Notable companies leading these advancements include Murata Manufacturing, TDK Corporation, and Samsung Electro-Mechanics.

## Data availability

No primary research results, software or code have been included and no new data were generated or analysed as part of this review.

## Conflicts of interest

There is no conflict of interest related to this publication

## Acknowledgements

## References

1 Electricity 2024 – Analysis - IEA, **https://www.iea.org/reports/electricity-2024**, (accessed 19 February 2024).

2 X. Luo, J. Wang, M. Dooner and J. Clarke, *Appl. Energy*, 2015, **137**, 511–536.

3 L. Pardo, F. Carmona, C. Alemany and B. Jimenez, *Ferroelectrics*, 1992, **134**, 77–82.

4 A. Stebnberg, *Ferroelectrics*, 1992, **134**, 29–34.

5 D. K. Das-gupta and Z. Shuren, *Ferroelectrics*, 1992, **134**, 71–76.

6 S. A. Sherrill, P. Banerjee, G. W. Rubloff and S. B. Lee, *Phys. Chem. Chem. Phys.*, 2011, **13**, 20714–20723.

7 Capacitor Bank Market Size, **https://www.gminsights.com/industry-analysis/capacitor-bank-market/market-size**, (accessed 20 March 2024).

8 D. V. Ragone, SAE Technical Papers, DOI: **10.4271/680453**.

9 SLC or MLCC Ceramic Capacitor: When it Fits Better?, **https://passive-components.eu/slc-or-mlcc-ceramic-capacitor-when-it-fits-better/**, (accessed 29 February 2024).

10 G. Liu, Y. Li, B. Guo, M. Tang, Q. Li, J. Dong, L. Yu, K. Yu, Y. Yan, D. Wang, L. Zhang, H. Zhang, Z. He and L. Jin, *Chem. Eng. J.*, 2021, **419**, 129673.

11 Lead Zirconate Titanate Market Size Report, 2021-2026, **https://www.industryarc.com/Report/16050/lead-zirconate-titanate-market.html**, (accessed 18 March 2024).

12 Y. Chen, D. Zhang, Z. Peng, M. Yuan and X. Ji, *Front. Mater.*, 2021, **8**, 679167.

13 Knowles Precision Devices Capacitors For Electric Vehicles, **https://info.knowlescapacitors.com/knowles-precision-devices-capacitors-for-electric-vehicles**, (accessed 29 February 2024).

**10784** | *Chem. Soc. Rev.*, 2024, **53**, 10761–10790

This journal is © The Royal Society of Chemistry 2024

14 Multi-layer Ceramic Capacitor (MLCC) Market to Reach $16.77 Billion by 2030 - Y5V Segment Anticipated to Register Noteworthy Growth, Marking It as an Area Ripe for Opportunities, https://shorturl.at/7NaAl (accessed 29 February 2024).

15 J. W. Park, J. H. Chae, I. H. Park, H. J. Youn and Y. H. Moon, *J. Am. Ceram. Soc.*, 2007, **90**, 2151–2158.

16 S. C. Das, A. Majumdar, A. Shahee, N. P. Lalla, T. Shripathi and R. Hippler, *Ferroelectr. Lett.Sect.*, 2011, **38**, 78–85.

17 X. Hao, *J. Adv. Dielectr.*, 2013, **3**(01), 1330001.

18 S. C. Abrahams, S. K. Kurtz and P. B. Jamieson, *Phys. Rev.*, 1968, **172**(2), 551.

19 Y. Shimakawa, Y. Kubo, Y. Nakagawa, S. Goto, T. Kamiyama and H. Asano, *Phys. Rev. B: Condens. Matter Mater. Phys.*, 2000, **61**, 6559.

20 H. Zhang, M. Krynski, A. D. Fortes, T. G. Saunders, M. Palma, Y. Hao, F. Krok, H. Yan and I. Abrahams, *J. Am. Chem. Soc.*, 2024, **146**, 5569–5579.

21 X. Tang, Z. Hu, V. Koval, B. Yang, G. Smith and H. Yan, *Chem. Eng. J.*, 2023, **473**, 145363.

22 Z. Chen, S. Mao, L. Ma, G. Luo, Q. Feng, Z. Cen, F. Toyohisa, X. Peng, L. Liu, H. Zhou, C. Hu and N. Luo, *J. Materiomics*, 2022, **8**, 753–762.

23 Z. Pan, L. Yao, G. Ge, B. Shen and J. Zhai, *J. Mater. Chem. A*, 2018, **6**, 14614–14622.

24 H. D. Megaw, *Ferroelectrics*, 1974, **7**, 87–89.

25 X. Tan, C. Ma, J. Frederick, S. Beckman and K. G. Webber, *J. Am. Ceram. Soc.*, 2011, **94**, 4091–4107.

26 M. Ahtee, A. M. Glazer and H. D. Megaw, *Philos. Mag.*, 1972, **26**, 995–1014.

27 L. Eric Cross, *Ferroelectrics*, 1987, **76**, 241–267.

28 J. Ma, Y. Lin, H. Yang and J. Tian, *J. Alloys Compd.*, 2021, **868**, 159206.

29 G. Wang, Z. Lu, Y. Li, L. Li, H. Ji, A. Feteira, D. Zhou, D. Wang, S. Zhang and I. M. Reaney, *Chem. Rev.*, 2021, **121**, 6124–6172.

30 H. Qi, A. Xie, A. Tian and R. Zuo, *Adv. Energy Mater.*, 2020, **10**(6), 1903338.

31 P. Nong, Y. Pan, Q. Dong, D. Zeng, M. Xu, X. Wang, J. Wang, L. Deng, X. Chen and H. Zhou, *Electron. Mater. Lett.*, 2023, **1**, 1–13.

32 X. Wang, H. Chen, Y. Pan, Q. Dong, J. Wang, X. Chen and H. Zhou, *J. Power Sources*, 2023, **566**, 232934.

33 L. Ma, Z. Chen, G. Luo, Z. Che, C. Xu, D. Shan, Z. Cen, Q. Feng, X. Chen, T. Fujita, Y. Zhu, Y. Liu, J.-F. Li, S. Zhang and N. Luo, *J. Materiomics*, 2024, **10**(5), 1026–1035.

34 Y. Fan, Z. Zhou, R. Liang, M. Zhou and X. Dong, *J. Eur. Ceram. Soc.*, 2019, **39**, 4712–4718.

35 A. Yadav, I. P. Raevski and P. M. Sarun, *Mater. Today Commun.*, 2022, **33**, 104712.

36 F. Ye, X. Jiang, X. Huang, R. Zeng, C. Chen, X. Nie and H. Cheng, *J. Mater. Sci.: Mater. Electron.*, 2022, **33**, 4497–4509.

37 A. Yadav, S. Sahoo, S. Singh, I. P. Raevski and P. M. Sarun, *Mater. Sci. Eng., B*, 2023, **297**, 116796.

38 W. Yang, H. Zeng, F. Yan, J. Lin, G. Ge, Y. Cao, W. Du, K. Zhao, G. Li, H. Xie and J. Zhai, *J. Mater. Chem. A*, 2022, **10**, 11613–11624.

39 J. Ye, G. Wang, M. Zhou, N. Liu, X. Chen, S. Li, F. Cao and X. Dong, *J. Mater. Chem C*, 2019, **7**(19), 5639–5645.

40 C. S. Htet, A. M. Manjón-Sanz, J. Liu, C. Babori, M. Barati, F. P. Marlton, L. Daniel, M. R. V. Jørgensen and A. Pramanick, *J. Eur. Ceram. Soc.*, 2024, **44**, 1597–1609.

41 X. Dong, X. Li, X. Chen, H. Chen, C. Sun, J. Shi, F. Pang and H. Zhou, *Ceram. Int.*, 2021, **47**, 3079–3088.

42 A. Xie, J. Fu, R. Zuo, C. Zhou, Z. Qiao, T. Li and S. Zhang, *Chem. Eng. J.*, 2022, **429**, 132534.

43 W. Xiao, Z. Liu, C. Zhang, Z. Dou, B. Fan, M. Shen, Y. Yang, W. Luo, K. Li, Q. Fu, S. Jiang, Y. Wang and G. Zhang, *Chem. Eng. J.*, 2023, **461**, 142070.

44 D. Yang, Y. Wang, X. Wang, C. Chen, L. Li, M. Yao, L. Miao, R. Ma, H. Cheng and D. Hu, *Ceram. Int.*, 2023, **49**, 7814–7822.

45 R. Muhammad, A. Ali, J. Camargo, M. S. Castro, W. Lei, K. Song and D. Wang, *Crystals*, 2022, **12**, 141.

46 J. Fu, H. Qi, A. Xie, A. Tian and R. Zuo, *Acta Mater.*, 2021, **215**, 117100.

47 L. Wang, S. Sun, H. Luo, Y. Ren, H. Liu, X. Xing and J. Chen, *J. Mater. Chem. A*, 2021, **9**, 2367–2374.

48 G. Liu, L. Chen and H. Qi, *Microstructures*, 2023, 3; G. Liu, L. Chen and H. Qi, *Chem. Eng. J.*, 2019, 3, 2023009.

49 M. H. Zhang, H. Ding, S. Egert, C. Zhao, L. Villa, L. Fulanović, P. B. Groszewicz, G. Buntkowsky, H. J. Kleebe, K. Albe, A. Klein and J. Koruza, *Nat. Commun.*, 2023, **14**, 1–11.

50 S. Zhang, W. Li, Y. Zhang, X. Tang, Y. Jiang and X. Guo, *Mater. Sci. Eng., B*, 2024, **299**, 117025.

51 P. Nong, D. Zeng, Y. Pan, Q. Dong, M. Xu, X. Wang, J. Wang, H. Zhou, X. Li and X. Chen, *J. Materiomics*, 2019, **10**(3), 670–681.

52 M. H. Zhang, L. Fulanović, C. Zhao and J. Koruza, *J. Materiomics*, 2023, **9**, 1–18.

53 J. Joseph, Z. Cheng and S. Zhang, *J. Materiomics*, 2022, **8**, 731–738.

54 Z. Wang, J. Zhao, G. Niu, N. Zhang, K. Zheng, Y. Quan, L. Wang, J. Zhuang, G. Wang, X. Li, H. Cai, M. Liu, Z. Jiang, Y. Zhao and W. Ren, *J. Eur. Ceram. Soc.*, 2023, **43**, 5511–5520.

55 J. Ma, J. Zhang, J. Guo, X. Li, S. Guo, Y. Huan, J. Wang, S. T. Zhang and Y. Wang, *Chem. Mater.*, 2022, **34**, 7313–7322.

56 V. M. Goldschmidt, *Naturwissenschaften*, 1926, **14**, 477–485.

57 H. Shimizu, H. Guo, S. E. Reyes-Lillo, Y. Mizuno, K. M. Rabe and C. A. Randall, *Dalton Trans.*, 2015, **44**, 10763–10772.

58 C. Liang, C. Wang, W. Cao, H. Zhao, F. Li and C. Wang, *J. Adv. Dielectr.*, 2023, **13**, 2242004.

59 M. Xu, X. Wang, P. Nong, D. Zeng, Q. Dong, Y. Pan, J. Wang, H. Zhou and X. Chen, *ACS Appl. Energy Mater.*, 2023, **6**, 1630–1638.

60 R. Kang, Z. Wang, W. Yang, X. Zhu, P. Shi, Y. Gao, P. Mao, J. Zhao, L. Zhang and X. Lou, *J. Mater. Chem. A*, 2021, **9**, 24387–24396.

This journal is © The Royal Society of Chemistry 2024

*Chem. Soc. Rev.*, 2024, **53**, 10761–10790 | **10785**

61 H. Chen, J. Shi, X. Chen, C. Sun, F. Pang, X. Dong, H. Zhang and H. Zhou, *J. Mater. Chem. A*, 2021, **9**, 4789–4799.

62 H. Li, Z. Pan, X. Chen, J. Zhao, L. Tang, J. Liu, P. Li and J. Zhai, *Mater. Today Phys.*, 2023, **38**, 101208.

63 J. Jiang, X. Meng, L. Li, J. Zhang, S. Guo, J. Wang, X. Hao, H. Zhu and S. T. Zhang, *Chem. Eng. J.*, 2021, **422**, 130130.

64 H. Qi, R. Zuo, A. Xie, A. Tian, J. Fu, Y. Zhang, S. Zhang, H. Qi, R. Z. Zuo, A. W. Xie, A. Tian, J. Fu, Y. Zhang and S. J. Zhang, *Adv. Funct. Mater.*, 2019, **29**, 1903877.

65 J. Ma, D. Zhang, F. Ying, X. Li, L. Li, S. Guo, Y. Huan, J. Zhang, J. Wang and S. T. Zhang, *ACS Appl. Mater. Interfaces*, 2022, **14**, 19704–19713.

66 T. Pan, J. Zhang, Z. N. Guan, Y. Yan, J. Ma, X. Li, S. Guo, J. Wang and Y. Wang, *Adv. Electron. Mater.*, 2022, **8**, 2200793.

67 D. Fu, M. Endo, H. Taniguchi, T. Taniyama and M. Ltoh, *Appl. Phys. Lett.*, 2007, **90**, 252907.

68 L. Zhao, Q. Liu, S. Zhang and J. F. Li, *J. Mater. Chem. C*, 2016, **4**, 8380–8384.

69 Z. Zheng, Y. Yang, L. Zhao, K. Zhu, H. Yang and J. Wang, *Ceram. Int.*, 2024, **50**, 3902–3911.

70 H. Yuan, X. Fan, Z. Zheng, M. Zhao, L. Zhao, K. Zhu and J. Wang, *Chem. Eng. J.*, 2023, **456**, 141023.

71 L. F. Zhu, S. Deng, L. Zhao, G. Li, Q. Wang, L. Li, Y. Yan, H. Qi, B. P. Zhang, J. Chen and J. F. Li, *Nat. Commun.*, 2023, **14**(1), 1166.

72 M. Zhao, J. Wang, J. Zhang, L. F. Zhu and L. Zhao, *J. Adv. Ceram.*, 2023, **12**, 1166–1177.

73 M. Zhao, J. Wang, H. Yuan, Z. Zheng and L. Zhao, *J. Materiomics*, 2023, **9**, 19–26.

74 L. Wang, Z. Zheng, H. Yuan, Y. Yang, J. Zhang, K. Zhu, X. Hu and J. Wang, *J. Eur. Ceram. Soc.*, 2024, **44**, 2934–2943.

75 Z. Lu, W. Bao, G. Wang, S. K. Sun, L. Li, J. Li, H. Yang, H. Ji, A. Feteira, D. Li, F. Xu, A. K. Kleppe, D. Wang, S. Y. Liu and I. M. Reaney, *Nano Energy*, 2021, **79**, 105423.

76 Y. Tian, J. Li, Q. Hu, K. Yu, Y. Zhuang, G. Viola, I. Abrahams, Z. Xu, X. Wei, H. Yan, C. Y. Tian, L. Jin, Q. Hu, K. Yu, Y. Zhuang, G. Viola, I. Abrahams, Z. Xu, X. Wei and H. Yan, *J. Mater. Chem. A*, 2019, **7**(2), 834–842.

77 J. Wang, X. Fan, Z. Liu, K. Zhu, H. Yuan, Z. Zheng, L. Zhao, J. Zhang, Q. Yuan and J. F. Li, *J. Mater. Chem. A*, 2023, **11**, 22512–22521.

78 S. Li, T. Hu, H. Nie, Z. Fu, C. Xu, F. Xu, G. Wang and X. Dong, *Energy Storage Mater.*, 2021, **34**, 417–426.

79 Y. Xu, Z. Yang, K. Xu, J. Tian, D. Zhang, M. Zhan, H. Tian, X. Cai, B. Zhang, Y. Yan, L. Guo, G. Wang, L. Lin, J. Fan, T. Wang and Y. Tian, *J. Alloys Compd.*, 2022, **913**, 165313.

80 Y. Xu, Z. Yang, K. Xu, Y. Cao, Y. Tian, L. Guo, J. Tian, H. Tian, X. Liu, L. Lin and G. Wang, *Chem. Eng. J.*, 2021, **426**, 131047.

81 Z. Lu, D. Sun, G. Wang, J. Zhao, B. Zhang, D. Wang and I. Shyha, *J. Adv. Dielectr.*, 2023, **13**, 2242006.

82 J. Zhou, J. Du, L. Chen, Y. Li, L. Xu, Q. Zhao, H. Yang, J. Ding, Z. Sun, X. Hao and X. Wang, *J. Eur. Ceram. Soc.*, 2023, **43**, 6059–6068.

83 X. Fan, J. Wang, H. Yuan, L. Chen, L. Zhao and K. Zhu, *ACS Appl. Mater. Interfaces*, 2022, **14**, 7052–7062.

84 B. Li, Z. Yan, X. Zhou, H. Qi, V. Koval, X. Luo, H. Luo, H. Yan and D. Zhang, *ACS Appl. Mater. Interfaces*, 2023, **15**, 4246–4256.

85 S. Gao, Y. Huang, Y. Jiang, M. Shen, H. Huang, S. Jiang, Y. He and Q. Zhang, *Acta Mater.*, 2023, **246**, 118730.

86 G. Wang, Z. Lu, Z. Zhang, A. Feteria, C. Tang and D. A. Halls, *J. Am. Ceram. Soc.*, 2019, **102**(12), 7746–7754, DOI: [10.1111/jace.16676](10.1111/jace.16676).

87 F. Yang, P. Wu and D. C. Sinclair, *Solid State Ionics*, 2017, **299**, 38–45.

88 Z. Pan, D. Hu, Y. Zhang, J. Liu, B. Shen and J. Zhai, *J. Mater. Chem. C*, 2019, **7**, 4072–4078.

89 H. Ji, D. Wang, W. Bao, Z. Lu, G. Wang, H. Yang, A. Mostaed, L. Li, A. Feteira, S. Sun, F. Xu, D. Li, C. J. Ma, S. Y. Liu and I. M. Reaney, *Energy Storage Mater.*, 2021, **38**, 113–120.

90 A. Khan, N. S. Gul, M. Luo, J. Wu, S. Z. Khan, A. Manan, X. J. Wang and T. M. Khan, *Front. Chem.*, 2022, **10**, 1025030.

91 B. J. Chu, D. R. Chen, G. R. Li and Q. R. Yin, *J. Eur. Ceram. Soc.*, 2002, **22**, 2115.

92 K. Liu, Y. Zhang, M. A. Marwat, G. Wang, D. Wang, W. Ma, T. Wei, M. li, J. Xu, H. Yang, S. Kongparakul, C. Samart, J. Zang, P. Fan and H. Zhang, *J. Am. Ceram. Soc.*, 2020, **103**, 3739–3747.

93 E. Aksel, J. S. Forrester, J. L. Jones, P. A. Thomas, K. Page and M. R. Suchomel, *Appl. Phys. Lett.*, 2011, **15**, 98.

94 K. Datta, P. Thomas and K. Roleder, *Phys. Rev. B: Condens. Matter Mater. Phys.*, 2010, **82**(22), 224105.

95 M. Li, M. J. Pietrowski, R. A. De Souza, H. Zhang, I. M. Reaney, S. N. Cook, J. A. Kilner and D. C. Sinclair, *Nat. Mater.*, 2014, **13**, 31–36.

96 A. P. Hoang, S. Steiner, F. Yang, L. Li, D. C. Sinclair and T. Fromling, *J. Am. Ceram. Soc.*, 2021, **14**(4), 2587–2595.

97 R. Sahu, R. R. Negi, B. Samanta, D. Nanda and P. Kumar, *J. Mater. Sci.: Mater. Electron.*, 2021, **32**, 17524–17533.

98 J. S. Kim, B. C. Choi, J. H. Jeong, K. S. Lee and S. B. Cho, *Ferroelectrics*, 2009, **384**, 120–125.

99 G. Liu, L. Hu, Y. Wang, Z. Wang, L. Yu, J. Lv, J. Dong, Y. Wang, M. Tang, B. Guo, K. Yu and Y. Yan, *Ceram. Int.*, 2020, **46**, 19375–19384.

100 S. Lenka, T. Badapanda, S. P. Ghosh, T. Richhariya, S. Sarangi and S. N. Tripathy, *Mater. Today Commun.*, 2023, **36**, 106738.

101 X. Qiao, F. Zhang, D. Wu, B. Chen, X. Zhao, Z. Peng, X. Ren, P. Liang, X. Chao and Z. Yang, *Chem. Eng. J.*, 2020, **388**, 124158.

102 W. Q. Luo, Z. Y. Shen, Y. Y. Yu, F. S. Song, Z. M. Wang and Y. M. Li, DOI: [10.1142/S2010135X18200047](10.1142/S2010135X18200047).

103 H. Borkar, V. N. Singh, B. P. Singh, M. Tomar, V. Gupta and A. Kumar, *RSC Adv.*, 2014, **4**, 22840–22847.

104 J. Wu, A. Mahajan, L. Riekehr, H. Zhang, B. Yang, N. Meng, Z. Zhang and H. Yan, *Nano Energy*, 2018, **50**, 723–732.

10786 | *Chem. Soc. Rev.*, 2024, **53**, 10761–10790

This journal is © The Royal Society of Chemistry 2024

105 L. Zhang, Y. Pu, M. Chen, T. Wei and X. Peng, *Chem. Eng. J.*, 2020, **383**, 123154.

106 Z. Liu, A. Zhang, S. Xu, J. Lu, B. Xie, K. Guo and Y. Mao, *J. Alloys Compd.*, 2020, **823**, 153772.

107 W. Cao, W. Li, T. Zhang, J. Sheng, Y. Hou, Y. Feng, Y. Yu and W. Fei, *Energy Technol.*, 2015, **3**, 1198–1204.

108 D. Hu, Z. Pan, X. Zhang, H. Ye, Z. He, M. Wang, S. Xing, J. Zhai, Q. Fu and J. Liu, *J. Mater. Chem. C*, 2020, **8**, 591–601.

109 K. R. Kandula, K. Banerjee, S. S. K. Raavi and S. Asthana, *Phys. Status Solidi A*, 2004, **16**(26), 5610–5615.

110 A. Kumar, R. Kumar, K. Singh and S. Singh, *Phys. Status Solidi A*, 2021, 1–79.

111 P. Chen, L. Zhang, J. Cai, Z. Wang, W. Shi, J. Jing, F. Wei, G. Liu, Y. Yan, H. Liu and L. Jin, *J. Mater. Sci.: Mater. Electron.*, 2019, **30**, 13556–13566.

112 C. Cui, Y. Pu and R. Shi, *J. Alloys Compd.*, 2018, **740**, 1180–1187.

113 C. Wang, F. Yan, H. Yang, Y. Lin and T. Wang, *J. Alloys Compd.*, 2018, **749**, 605–611.

114 J. Li, F. Li, Z. Xu and S. Zhang, *Adv. Mater.*, 2021, **90**, 106528.

115 F. Yang, M. Li, L. Li, P. Wu, E. Pradal-Velázquez and D. C. Sinclair, *J. Mater. Chem. A*, 2018, **6**, 5243–5254.

116 D. P. C. Shih, A. Aguadero and S. J. Skinner, *J. Am. Ceram. Soc.*, 2023, **106**, 100–108.

117 J. Suchanicz, M. Wąs, M. Nowakowska-Malczyk, D. Sitko, K. Kluczewska-Chmielarz, K. Konieczny, G. Jagło, P. Czaja, B. Handke, Z. Kucia, P. Zając and K. Łyszczarz, *Materials*, 2022, **15**(18), 6204.

118 W.-Q. Luo, Z.-Y. Shen, Y.-Y. Yu, F.-S. Song, Z.-M. Wang and Y.-M. Li, DOI: 10.1142/S2010135X18200047.

119 I. Tae, DOI: 10.1111/jace.16401.

120 W. P. Cao, J. Sheng, Z. Liu, C. Gao, Z. H. Wang, J. Wang, J. Chang, Z. Wang and W. L. Li, *Mod. Phys. Lett. B*, 2020, **34**(11), 2050100.

121 S. T. Zhang, F. Yan, B. Yang and W. Cao, *Appl. Phys. Lett.*, 2010, **97**(12), 1.

122 M. A. Rahman, *J. Asian Ceram. Soc.*, 2023, **11**, 215–224.

123 Y. S. Zhang, W. H. Li, X. G. Tang, K. Meng, S. Y. Zhang, X. Z. Xiao, X. Bin Guo, Y. P. Jiang and Z. Tang, *J. Alloys Compd.*, 2022, **911**, 165074.

124 L. Yang, X. Kong, Z. Cheng and S. Zhang, *J. Mater. Chem. A*, 2019, **7**, 8573–8580.

125 L. Zhang, Y. Pu and M. Chen, *Ceram. Int.*, 2020, **46**, 98–105.

126 Q. Xu, H. Liu, L. Zhang, J. Xie, H. Hao, M. Cao, Z. Yao and M. T. Lanagan, *RSC Adv.*, 2016, **6**, 59280–59291.

127 Z. Yang, Y. Yuan, L. Cao, E. Li and S. Zhang, *Ceram. Int.*, 2020, **46**, 11282–11289.

128 G. Liu, J. Dong, L. Zhang, L. Yu, F. Wei, Y. Li, J. Gao, J. Hu, Y. Yan, Q. Li, K. Yu and L. Jin, *Ceram. Int.*, 2020, **46**, 11680–11688.

129 L. Zhang, Y. Pu and M. Chen, *J. Alloys Compd.*, 2019, **775**, 342–347.

130 P. Chen and B. Chu, *J. Eur. Ceram. Soc.*, 2016, **36**, 81–88.

131 P. Butnoi, S. Manotham, P. Jaita, C. Randorn and G. Rujijanagul, *J. Eur. Ceram. Soc.*, 2018, **38**, 3822–3832.

132 J. Sui, H. Fan, B. Hu and L. Ning, *Ceram. Int.*, 2018, **44**, 18054–18059.

133 L. Zhang, Y. Pu, M. Chen, T. Wei, W. Keipper, R. Shi, X. Guo, R. Li and X. Peng, *J. Eur. Ceram. Soc.*, 2020, **40**, 71–77.

134 B. Hu, H. Fan, L. Ning, Y. Wen and C. Wang, *Ceram. Int.*, 2018, **44**, 15160–15166.

135 Y. Xu, Y. Hou, H. Zhao, M. Zheng and M. Zhu, *Mater. Lett.*, 2019, **249**, 21–24.

136 L. Zhang, Y. Pu, M. Chen, R. Li, X. Guo and Y. Cui, *Ceram. Int.*, 2018, **44**, S207–S210.

137 X. Liu, H. Yang, F. Yan, Y. Qin, Y. Lin and T. Wang, *J. Alloys Compd.*, 2019, **778**, 97–104.

138 J. Yin, X. Lv and J. Wu, *Ceram. Int.*, 2017, **43**, 13541–13546.

139 M. Yao, Y. Pu, L. Zhang and M. Chen, *Mater. Lett.*, 2016, **174**, 110–113.

140 P. Ren, Z. Liu, X. Wang, Z. Duan, Y. Wan, F. Yan and G. Zhao, *J. Alloys Compd.*, 2018, **742**, 683–689.

141 Y. Qiu, Y. Lin, X. Liu and H. Yang, *J. Alloys Compd.*, 2019, **797**, 348–355.

142 Y. Huang, F. Li, H. Hao, F. Xia, H. Liu and S. Zhang, *J. Materiomics*, 2019, **5**, 385–393.

143 R. Sahu, R. R. Negi, B. Samanta, D. Nanda and P. Kumar, *J. Mater. Sci.: Mater. Electron.*, 2021, **32**, 17524–17533.

144 S. Dagar, A. Hooda, S. Khasa and M. Malik, *Mater. Chem. Phys.*, 2020, **249**, 123214.

145 C. Wu, X. Qiu, C. Liu, H. Zhao, L. Chen, W. Ge and M. Yao, *Phys. Status Solidi A*, 2022, **219**, 2100737.

146 H. Wang, Q. Li, Y. Jia, A. K. Yadav, B. Yan, Q. Shen, M. Li, Q. Quan and H. Fan, *J. Mater. Sci.*, 2021, **56**, 14672–14683.

147 Y. Qiao, W. Li, Y. Zhao, Y. Zhang, W. Cao and W. Fei, *ACS Appl. Energy Mater.*, 2018, **1**, 956–962.

148 J. A. Dawson, H. Chen and I. Tanaka, *J. Mater. Chem. A*, 2015, **3**, 16574–16582.

149 X. He and Y. Mo, *Phys. Chem. Chem. Phys.*, 2015, **17**, 18035–18044.

150 C. Wu, X. Qiu, W. Ge, C. Liu, H. Zhao, L. Chen, Z. Liu, L. Li and J. G. Fisher, *Ceram. Int.*, 2022, **48**, 31931–31940.

151 X. Zhang, F. Yang, W. Miao, Z. Su, J. Zhao, L. Tang, Y. Shen, D. Hu, Y. Chen, P. Li, J. Liu and Z. Pan, *J. Alloys Compd.*, 2021, **883**, 160837.

152 Z. Jiang, Z. Yang, Y. Yuan, B. Tang and S. Zhang, *J. Alloys Compd.*, 2021, **851**, 156821.

153 A. M. Balakt, C. P. Shaw and Q. Zhang, *J. Alloys Compd.*, 2017, **709**, 82–91.

154 T. Zhao, K. Shi, C. Fei, X. Sun, Y. Quan, W. Liu, J. Zhang and X. Dai, *Crystals*, 2023, **13**, 433.

155 X. P. Jiang, X. L. Fu, C. Chen, N. Tu, M. Z. Xu, X. H. Li, H. Shao and Y. J. Chen, *J. Adv. Ceram.*, 2015, **4**, 54–60.

156 J. Xi, J. Xing, H. Chen, F. Zhang, Q. Chen, W. Zhang and J. Zhu, *J. Alloys Compd.*, 2021, **868**, 159216.

157 H. Guo, Y. Li, Y. Zhang, H. Sun and X. Liu, *J. Mater. Sci.: Mater. Electron.*, 2018, **29**, 19063–19069.

This journal is © The Royal Society of Chemistry 2024

*Chem. Soc. Rev.*, 2024, **53**, 10761–10790 | **10787**

158  W. Cao, R. Lin, X. Hou, L. Li, F. Li, D. Bo, B. Ge, D. Song, J. Zhang, Z. Cheng and C. Wang, *Adv. Funct. Mater.*, 2023, **33**, 2301027.

159  D. Li, D. Xu, W. Zhao, M. Avdeev, H. Jing, Y. Guo, T. Zhou, W. Liu, D. Wang and D. Zhou, *Energy Environ. Sci.*, 2023, **16**, 4511–4521.

160  J. Yin, X. Shi, H. Tao, Z. Tan, X. Lv, X. Ding, J. Sun, Y. Zhang, X. Zhang, K. Yao, J. Zhu, H. Huang, H. Wu, S. Zhang and J. Wu, *Nat. Commun.*, 2022, **13**, 1–9.

161  H. Liu, Z. Sun, J. Zhang, H. Luo, Q. Zhang, Y. Yao, S. Deng, H. Qi, J. Liu, L. C. Gallington, J. C. Neuefeind and J. Chen, *J. Am. Chem. Soc.*, 2023, **145**, 11764–11772.

162  H. Liu, Z. Sun, J. Zhang, H. Luo, Y. Yao, X. Wang, H. Qi, S. Deng, J. Liu, L. C. Gallington, Y. Zhang, J. C. Neuefeind and J. Chen, *J. Am. Chem. Soc.*, 2023, **145**, 19396–19404.

163  M. Jiang, Z. Peng, Q. Zhou, D. Wu, L. Wei, P. Liang, X. Chao and Z. Yang, DOI: [10.1142/S2010135X23400052](10.1142/S2010135X23400052).

164  K. Wang, W. Li, X. Tang, S. Zhang, Y. Zhang, J. Hu, Z. Shen, Y. Jiang and X. Guo, *J. Adv. Dielectr.*, 2023, **13**, 2350008.

165  D. Li, D. Zhou, D. Wang, W. Zhao, Y. Guo, Z. Shi, T. Zhou, S. K. Sun, C. Singh, S. Trukhanov and A. S. B. Sombra, *Small*, 2023, **19**, 2206958.

166  X. Zhu, Y. Gao, P. Shi, R. Kang, F. Kang, W. Qiao, J. Zhao, Z. Wang, Y. Yuan and X. Lou, *Nano Energy*, 2022, **98**, 107276.

167  M. Wang, Q. Feng, C. Luo, Y. Lan, C. Yuan, N. Luo, C. Zhou, T. Fujita, J. Xu, G. Chen and Y. Wei, *ACS Appl. Mater. Interfaces*, 2021, **13**, 51218–51229.

168  W. Zhao, D. Xu, D. Li, M. Avdeev, H. Jing, M. Xu, Y. Guo, D. Shi, T. Zhou, W. Liu, D. Wang and D. Zhou, *Nat. Commun.*, 2023, **14**, 1–11.

169  T. Li, X. Jiang, J. Li, A. Xie, J. Fu and R. Zuo, *ACS Appl. Mater. Interfaces*, 2022, **14**, 22263–22269.

170  H. Liu, Z. Sun, J. Zhang, H. Luo, Q. Zhang, Y. Yao, S. Deng, H. Qi, J. Liu, L. C. Gallington, J. C. Neuefeind and J. Chen, *J. Am. Chem. Soc.*, 2023, **145**, 11764–11772.

171  L. Chen, H. Yu, J. Wu, S. Deng, H. Liu, L. Zhu, H. Qi and J. Chen, *Nanomicro Lett.*, 2023, **15**, 1–14.

172  S. Kim, H. Nam and I. Calisir, *Materials*, 2022, **15**, 4388.

173  J. B. Neaton, C. Ederer, U. V. Waghmare, N. A. Spaldin and K. M. Rabe, *Phys. Rev. B: Condens. Matter Mater. Phys.*, 2005, **71**, 014113.

174  N. Liu, R. Liang, Z. Zhou and X. Dong, *J. Mater. Chem. C*, 2018, **6**, 10211–10217.

175  S. Kharbanda, N. Dhanda, A. C. Aidan Sun, A. Thakur and P. Thakur, *J. Magn. Magn. Mater.*, 2023, **572**, 170569.

176  Z. N. Guan, Y. Yan, J. Ma, T. Pan, X. Li, S. Guo, J. Zhang, J. Wang and Y. Wang, *ACS Appl. Mater. Interfaces*, 2022, **14**, 44539–44549.

177  D. Wang, Z. Fan, D. Zhou, A. Khesro, S. Murakami, A. Feteira, Q. Zhao, X. Tan and I. M. Reaney, *J. Mater. Chem. A*, 2018, **6**, 4133–4144.

178  L. Wang, D. Zhou and A. Feteira, DOI: [10.1021/acsaem.8b01099](10.1021/acsaem.8b01099).

179  G. Wang, Z. Lu, J. Li, H. Ji, H. Yang, L. Li, S. Sun, A. Feteira, H. Yang, R. Zuo, D. Wang and I. M. Reaney, *J. Eur. Ceram. Soc.*, 2020, **40**, 1779–1783.

180  T. Wu, W. Zhang, F. Liu, Z. Dou, S. Han, P. Fan, S. G. Chen, C. Samart, D. Salamon, H. Tan and H. Zhang, *Ceram. Int.*, 2023, **49**, 1820–1825.

181  G. Wang, J. Li, X. Zhang, Z. Fan, F. Yang, A. Feteira, D. Zhou, D. C. Sinclair, T. Ma, X. Tan, D. Wang and I. M. Reaney, *Energy Environ. Sci.*, 2019, **12**, 582–588.

182  T. Cui, J. Zhang, J. Guo, X. Li, S. Guo, Y. Huan, J. Wang and S. T. Zhang, *J. Mater. Chem. A*, 2022, **10**, 14316–14325.

183  X. Wang, Y. Fan, B. Zhang, A. Mostaed, L. Li, A. Feteira, D. Wang, D. C. Sinclair, G. Wang and I. M. Reaney, *J. Eur. Ceram. Soc.*, 2022, **42**, 7381–7387.

184  F. Yan, H. Bai, G. Ge, J. Lin, C. Shi, K. Zhu, B. Shen, J. Zhai, S. Zhang, F. Yan, H. R. Bai, G. L. Ge, J. F. Lin, C. Shi, K. Zhu, B. Shen, J. W. Zhai and S. J. Zhang, *Small*, 2022, **18**, 2106515.

185  H. Sun, X. Wang, Q. Sun, X. Zhang, Z. Ma, M. Guo, B. Sun, X. Zhu, Q. Liu and X. Lou, *J. Eur. Ceram. Soc.*, 2020, **40**, 2929–2935.

186  A. Khesro, F. A. Khan, R. Muhammad, A. Ali, M. Khan and D. Wang, *Ceram. Int.*, 2022, **48**, 29938–29943.

187  H. Yang, H. Qi and R. Zuo, *J. Eur. Ceram. Soc.*, 2019, **39**, 2673–2679.

188  F. Kang, L. Zhang, W. Yang, R. Kang, R. Xue, L. He, Q. Sun, T. Zhang, Z. Wang, J. Wang and K. Zeng, *J. Eur. Ceram. Soc.*, 2022, **42**, 6958–6967.

189  F. Yan, Y. Shi, X. Zhou, K. Zhu, B. Shen and J. Zhai, *Chem. Eng. J.*, 2021, **417**, 127945.

190  R. Montecillo, J. C. Lin, C. S. Chen, P. Y. Chen and C. S. Tu, *J. Alloys Compd.*, 2023, **963**, 171144.

191  R. Montecillo, C. S. Chen, K. C. Feng, R. R. Chien, S. C. Haw, P. Y. Chen and C. S. Tu, *J. Eur. Ceram. Soc.*, 2023, **43**, 7446–7454.

192  Z. Lu, G. Wang, W. Bao, J. Li, L. Li, A. Mostaed, H. Yang, H. Ji, D. Li, A. Feteira, F. Xu, D. C. Sinclair, D. Wang, S. Y. Liu and I. M. Reaney, *Energy Environ. Sci.*, 2020, **13**, 2938–2948.

193  T. Cui, J. Zhang, J. Guo, X. Li, S. Guo, Y. Huan, J. Wang, S. T. Zhang and Y. Wang, *Acta Mater.*, 2022, **240**, 118286.

194  K. Hong, T. H. Lee, J. M. Suh, S. H. Yoon and H. W. Jang, *J. Mater. Chem. C*, 2019, **7**, 9782–9802.

195  Multi-layer Ceramic Capacitor (MLCC) Market to Reach $16.77 Billion by 2030 - Y5V Segment Anticipated to Register Noteworthy Growth, Marking It as an Area Ripe for Opportunities, [https://uk.finance.yahoo.com/news/multi-layer-ceramic-capacitor-mlcc-233800598.html](https://uk.finance.yahoo.com/news/multi-layer-ceramic-capacitor-mlcc-233800598.html), (accessed 5 March 2024).

196  Main applications and examples of use | Polymer Aluminum Electrolytic Capacitors | Murata Manufacturing Co., Ltd., [https://www.murata.com/en-eu/products/capacitor/polymer/overview/basic/use-case](https://www.murata.com/en-eu/products/capacitor/polymer/overview/basic/use-case), (accessed 5 March 2024).

197  Introduction to Multilayer Ceramic Capacitors and Practical Application Hints, [https://www.digikey.co.uk/en/maker/tutorials/2016/introduction-to-multilayer-ceramic-capacitors-and-practical-application-hints](https://www.digikey.co.uk/en/maker/tutorials/2016/introduction-to-multilayer-ceramic-capacitors-and-practical-application-hints), (accessed 5 March 2024).

198  W.-B. Li, D. Zhou, R. Xu, L.-X. Pang and I. M. Reaney, DOI: [10.1021/acsaem.8b01001](10.1021/acsaem.8b01001).

**10788** | *Chem. Soc. Rev.*, 2024, **53**, 10761–10790

This journal is © The Royal Society of Chemistry 2024

199 L. F. Zhu, L. Zhao, Y. Yan, H. Leng, X. Li, L. Q. Cheng, X. Xiong and S. Priya, *J. Mater. Chem. A*, 2021, **9**, 9655–9664.

200 Z. Lv, T. Lu, Z. Liu, T. Hu, Z. Hong, S. Guo, Z. Xu, Y. Song, Y. Chen, X. Zhao, Z. Lin, D. Yu, Y. Liu and G. Wang, *Adv. Energy Mater.*, 2024, **14**(12), 2304291.

201 G. Wang, Z. Lu, H. Yang, H. Ji, A. Mostaed, L. Li, Y. Wei, A. Feteira, S. Sun, D. C. Sinclair, D. Wang and I. M. Reaney, *J. Mater. Chem. A*, 2020, **8**, 11414–11423.

202 H. Wang, P. Zhao, L. Chen, L. Li and X. Wang, *J. Adv. Ceram.*, 2020, **9**, 292–302.

203 P. Zhao, Z. Cai, L. Chen, L. Wu, Y. Huan, L. Guo, L. Li, H. Wang and X. Wang, *Energy Environ. Sci.*, 2020, **13**, 4882–4890.

204 M. Zhang, S. Lan, B. B. Yang, H. Pan, Y. Q. Liu, Q. H. Zhang, J. L. Qi, D. Chen, H. Su, D. Yi, Y. Y. Yang, R. Wei, H. D. Cai, H. J. Han, L. Gu, C.-W. Nan and Y.-H. Lin, *Science*, 1979, **2024**(384), 185–189.

205 J. Li, Z. Shen, X. Chen, S. Yang, W. Zhou, M. Wang, L. Wang, Q. Kou, Y. Liu, Q. Li, Z. Xu, Y. Chang, S. Zhang and F. Li, *Nat. Mater.*, 2020, **19**, 999–1005.

206 Y. Zhou, J. Chen, N. Jiang, F. Guo, B. Yang and S. Zhao, *Chem. Eng. J.*, 2022, **431**, 133999.

207 Z. Pan, J. Ding, X. Hou, S. Shi, L. Yao, J. Liu, P. Li, J. Chen, J. Zhai and H. Pan, *J. Mater. Chem. A*, 2021, **9**, 9281–9290.

208 Z. Pan, P. Wang, X. Hou, L. Yao, G. Zhang, J. Wang, J. Liu, M. Shen, Y. Zhang, S. Jiang, J. Zhai, Q. Wang, Z. Pan, P. Wang, J. Liu, J. Zhai, X. Hou, J. Wang, L. Yao, G. Zhang, M. Shen, Y. Zhang, S. Jiang and Q. Wang, *Adv. Energy Mater.*, 2020, **10**, 2001536.

209 H. Pan, F. Li, Y. Liu, Q. Zhang, M. Wang, S. Lan, Y. Zheng, J. Ma, L. Gu, Y. Shen, P. Yu, S. Zhang, L. Q. Chen, Y. H. Lin and C. W. Nan, *Science*, 1979, **2019**(365), 578–582.

210 B. Yang, Y. Zhang, H. Pan, W. Si, Q. Zhang, Z. Shen, Y. Yu, S. Lan, F. Meng, Y. Liu, H. Huang, J. He, L. Gu, S. Zhang, L. Q. Chen, J. Zhu, C. W. Nan and Y. H. Lin, *Nat. Mater.*, 2022, **21**, 1074–1080.

211 Z. Liang, M. Liu, L. Shen, L. Lu, C. Ma, X. Lu, X. Lou and C. L. Jia, *ACS Appl. Mater. Interfaces*, 2019, **11**, 5247–5255.

212 H. Cheng, X. Zhai, J. Ouyang, L. Zheng, N. Luo, J. Liu, H. Zhu, Y. Wang, L. Hao and K. Wang, *J. Adv. Ceram.*, 2023, **12**, 196–206.

213 H. Pan, Y. Zeng, Y. Shen, Y. H. Lin, J. Ma, L. Li and C. W. Nan, *J. Mater. Chem. A*, 2017, **5**, 5920–5926.

214 Z. Liang, C. Ma, L. Shen, L. Lu, X. Lu, X. Lou, M. Liu and C. L. Jia, *Nano Energy*, 2019, **57**, 519–527.

215 C. Yang, P. Lv, J. Qian, Y. Han, J. Ouyang, X. Lin, S. Huang and Z. Cheng, *Adv. Energy Mater.*, 2019, **9**(18), 1803949.

216 Y. Fan, Z. Zhou, Y. Chen, W. Huang and X. Dong, *J. Mater. Chem. C*, 2019, **8**, 50–57.

217 X. Chen, B. Peng, M. J. Ding, X. Zhang, B. Xie, T. Mo, Q. Zhang, P. Yu and Z. L. Wang, *Nano Energy*, 2020, **78**, 105390.

218 F. Zhao, Y. Wu, Y. Dai, G. Hu, M. Liu, R. Gao, L. Liu, X. Liu, Y. Cheng, T. Y. Hu, C. Ma, D. Hu, X. Ouyang and C. L. Jia, *J. Mater. Chem. A*, 2021, **9**, 14818–14826.

219 K. Wang, J. Ouyang, M. Wuttig, Y. Y. Zhao, H. Cheng, Y. Zhang, R. Su, J. Yan, X. Zhong and F. Zeng, *Adv. Energy Mater.*, 2020, **10**(37), 2001778.

220 K. Wang, Y. Zhang, S. Wang, Y. Y. Zhao, H. Cheng, Q. Li, X. Zhong and J. Ouyang, *ACS Appl. Mater. Interfaces*, 2021, **13**, 22717–22727.

221 M. Randall, D. Skamser, T. Kinard, J. Qazi, A. Tajuddin, S. Trolier-Mckinstry, C. Randall, S. W. Ko and T. Dechakupt, academia.edu.

222 C. A. Randall and A. S. Bhalla, *Jpn J. Appl. Phys.*, 1990, **29**, 327–333.

223 T. Tsurumi, H. Adachi, H. Kakemoto, S. Wada, Y. Mizuno, H. Chazono and H. Kishi, *Jpn. J. Appl. Phys., Part 1*, 2002, **41**, 6929–6933.

224 M. J. Pan and C. Randall, *IEEE Electr. Insul. Mag.*, 2010, **26**, 44–50.

225 Main applications and examples of use | Polymer Aluminum Electrolytic Capacitors | Murata Manufacturing Co., Ltd., **https://www.murata.com/en-eu/products/capacitor/polymer/ overview/basic/use-case**, (accessed 29 February 2024).

226 D. Wang, Z. Fan, W. Li, D. Zhou, A. Feteira, G. Wang, S. Murakami, S. Sun, Q. Zhao, X. Tan and I. M. Reaney, *ACS Appl. Energy Mater.*, 2018, **1**, 4403–4412.

227 D. Hou, H. Fan, A. Zhang, Y. Chen, F. Yang, Y. Jia, H. Wang, Q. Quan and W. Wang, *Ceram. Int.*, 2021, **47**, 34059–34067.

228 Z. Yang, H. Du, L. Jin, Q. Hu, H. Wang, Y. Li, J. Wang, F. Gao and S. Qu.

229 W. A. Wani, N. Naaz, B. H. Venkataraman, S. Kundu and K. Ramaswamy, *J. Phys.: Conf. Ser.*, 2021, **2070**, 012088.

230 H. Liu and Y. Sun, *J. Phys. Chem. Solids*, 2022, **170**, 110951.

231 Y. Zhang, Y. Yao, J. Ren, H. Kong, B. Wang, Z. Wang, Z. Zhang and J. Wang, *J. Alloys Compd.*, 2020, **829**, 154546.

232 M. Q. Awan, J. Ahmad, A. Berlie, Q. Sun, R. L. Withers and Y. Liu, *Ceram. Int.*, 2018, **44**(11), 12767–12773.

233 S. Chao, F. D.-J. S. Chao and F. Dogan, *J. Am. Ceram. Soc.*, 2011, **94**, 179–186.

234 Z. Lu, G. Wang, W. Bao, J. Li, L. Li, A. Mostaed, H. Yang, H. Ji, D. Li, A. Feteira, F. Xu, D. C. Sinclair, D. Wang, S.-Y. Liu and I. M. Reaney, *Energy Environ. Sci.*, 2020, **13**, 2938.

235 H. Qin, J. Zhao, X. Chen, H. Li, S. Wang, Y. Du, P. Li, H. Zhou and D. Wang, *J. Adv. Dielectr.*, 2023, **13**(6), 2350018-1.

236 Y. Tian, L. Jin, H. Zhang, Z. Xu, X. Wei, E. D. Politova, S. Y. Stefanovich, N. V. Tarakina, I. Abrahams and H. Yan, *J. Mater. Chem. A*, 2016, **4**, 17279–17287.

237 R. Zuo, H. Qi and J. Fu, *Appl. Phys. Lett.*, 2016, **109**, 22902.

238 A. Sarkar, Q. Wang, A. Schiele, M. R. Chellali, S. S. Bhattacharya, D. Wang, T. Brezesinski, H. Hahn, L. Velasco and B. Breitung, *Adv. Mater.*, 2019, **31**, 1806236.

239 S. Murty, J. W. Yeh and S. Ranganathan, High-Entropy - Google Scholar, **https://scholar.google.com/scholar?hl= en&as_sdt=0%2C5&q=12B.+S.+Murty%2C+J.+W.+Yeh%2C+S. +Ranganathan%2C+High-Entropy+Alloys%2C+Butterworth- +Heinemann%2C+London+2014.&btnG=**, (accessed 19 May 2024).

240 L. Chen, S. Deng, H. Liu, J. Wu, H. Qi and J. Chen, *Nat. Commun.*, 2022, **13**, 1–8.

241 W. Petuskey, *Elsv.*, 1999.

This journal is © The Royal Society of Chemistry 2024

*Chem. Soc. Rev.*, 2024, **53**, 10761–10790 | **10789**

242 M. Prakasam, P. Veber, O. Viraphong, L. Etienne, M. Lahaye, S. Pechev, E. Lebraud, K. Shimamura and M. Maglione, *C. R. Phys.*, 2013, **14**(2–3), 133–140.

243 N. Reeves-McLaren, M. C. Ferrarelli, Y. W. Tung, D. C. Sinclair and A. R. West, *J. Solid State Chem.*, 2011, **184**(7), 1813–1819.

244 M. Lee and K. Kim, C. Y.-S. I. International J. 1986, ieeexplore.ieee.org.

245 Palladium Price in USD per Gram for Last 6 Months, **https://www.bullionbypost.eu/palladium-price/sixmonth/grams/USD/**, (accessed 3 April 2024).

246 F. Yan, J. Qian, J. Lin, G. Ge, C. Shi and J. Zhai, *Small*, 2024, **20**, 2306803.

247 Average prices for nickel worldwide 2014-2025 | Statista, **https://www.statista.com/statistics/675880/average-prices-nickel-worldwide/**, (accessed 3 April 2024).

248 G. Y. Yang, S. I. Lee, Z. J. Liu, C. J. Anthony, E. C. Dickey, Z. K. Liu and C. A. Randall, *Acta Mater.*, 2006, **54**, 3513–3523.

249 S. Dursun, A. E. Gurdal, S. Tuncdemir and C. Randall, *Sens. Actuators, A*, 2019, **286**, 4–13.

250 L. Tang, Z. Pan, J. Zhao, Y. Shen, X. Chen, H. Li, P. Li, Y. Zhang, J. Liu and J. Zhai, *J. Alloys Compd.*, 2023, **935**, 168124.

251 J. H. Kim, J. S. Kim, S. H. Han, H. W. Kang, H. G. Lee and C. I. Cheon, *Mater. Res. Bull.*, 2017, **96**, 121–125.

**10790** | *Chem. Soc. Rev.*, 2024, **53**, 10761–10790

This journal is © The Royal Society of Chemistry 2024